Article:
Li, J., Song, H., Bond, D.P.G. et al. (2026) On the causes of the end-Triassic mass extinction. Earth-Science Reviews, 279. 105542. ISSN: 0012-8252

https://doi.org/10.1016/j.earscirev.2026.105542

On the Causes of the End-Triassic Mass Extinction

Jing Li[a], Huyue Song[a*], David P.G. Bond[b], Paul B. Wignall[c], Yong Du[a], Haijun Song[a]

[a] State Key Laboratory of Geomicrobiology and Environmental Changes (GMEC) and School of Earth and Planetary Sciences, China University of Geosciences, Wuhan 430074, China

[b] School of Environmental and Life Sciences, University of Hull, Hull, HU6 7RX, UK

[c] School of Earth and Environment, University of Leeds, Leeds, LS2 9JT, UK

* Corresponding Author. *E-mail address:* hysong@cug.edu.cn.

Abstract:

The end-Triassic Mass Extinction (ETME) was one of the most severe biotic crises of the Phanerozoic. The ETME was marked by the extinction of conodonts and severe declines among ammonites, bivalves, brachiopods, and reef-building taxa. This catastrophe coincides with the emplacement of the Central Atlantic Magmatic Province (CAMP), suggesting a temporal and causal relationship. Additionally, globally distributed sedimentary mercury anomalies (Hg/TOC peaks and volcanogenic Δ^{199}Hg signals) further link volcanogenic Hg emissions to the ETME. A cascade of environmental disturbances triggered by CAMP volcanism through magmatic outgassing and contact metamorphism likely played a driving role in causing the

terrestrial and marine crises. Here, we review the extinction patterns of the ETME, CAMP-driven environmental and biogeochemical perturbations, and their synergistic causal relationships. Evidence indicates that the ETME occurred rapidly as a two-phased event within ~100 kyr. On land, ecosystem stress and collapse was marked by deforestation, extensive wildfires and acid rain together with global warming. This last factor intensified continental weathering and increased terrestrial runoff that likely promoted eutrophication and water-column stratification, ultimately causing the widespread marine anoxia/euxinia that is implicated in the marine crisis. Furthermore, these drivers also acted in concert to disrupt biogeochemical cycles (e.g., carbon, nitrogen, and sulfur), inducing a scarcity of bioavailable nitrogen and a drawdown of seawater sulfate concentrations that further stressed environments and ecosystems.

Keywords: Central Atlantic Magmatic Province; Global warming; Marine anoxia; Biogeochemical cycles; Triassic–Jurassic transition

1 Introduction

The Triassic Period culminated in one of the “big five” mass extinction events of the Phanerozoic, the end-Triassic mass extinction (ETME; ca. 201 Ma). Major shifts in ecological structures were underpinned by severe losses that occurred in all habitats throughout the marine realm and amongst many terrestrial communities (e.g. Hallam and Wignall, 1997; Hallam, 2002; Kiessling et al., 2007; Lathuilière and Marchal, 2009; Greene et al. 2012a; Dunhill et al., 2018; Allen et al., 2019; Wignall and Atkinson, 2020;

45 Larina et al., 2021). Marine ecosystems suffered catastrophic declines, with 23% of
46 families and 33% of genera lost globally (Deng et al., 2005). Extinction magnitudes are
47 severe in European successions, with species-level losses reaching 92% and genus-level
48 losses estimated at 42% among some groups (Hallam, 2002; Deng et al., 2005; Wignall
49 and Atkinson, 2020). Terrestrial biotas also experienced profound disruption, with
50 major turnovers seen in vertebrate faunas and plant communities, including the
51 extinction of several tetrapod lineages (Olsen et al., 1987, 2002; Kiessling et al., 2007;
52 Lucas and Tanner, 2015; Dunhill et al., 2018). The ETME reshaped the biosphere and
53 reset the evolutionary trajectory of life, leading to terrestrial environments dominated
54 by dinosaurs, and oceans with modern-style reef ecosystems (Olsen et al., 2002;
55 Toljagic and Butler, 2013; Allen et al., 2019).

56 Proposed kill mechanisms in ETME scenarios include a significant rise in
57 atmospheric pCO_2 and global warming (McElwain et al., 1999; Huynh and Poulsen,
58 2005; Bonis et al., 2010a; Capriolo et al., 2020, 2022; Song et al., 2021), ocean
59 acidification (van de Schootbrugge et al., 2007; Greene et al., 2012a; Ikeda et al., 2015;
60 Jost et al., 2017a; Kovács et al., 2022), anoxia in shallow marine settings and the
61 expansion of the oxygen minimum zone (OMZ; Bonis et al., 2010a; Jost et al., 2017b;
62 Fujisaki et al., 2020; Li et al., 2022; He et al. 2022a,b), and photic zone euxinia (PZE;
63 Richoz et al., 2012; Jaraula et al., 2013; Kasprak et al., 2015; Blumenberg et al., 2016;
64 Beith et al., 2021). The main driver of these stresses was likely the Central Atlantic
65 Magmatic Province (CAMP). The CAMP is one of the most voluminous large igneous
66 provinces (LIPs), the emplacement of which closely coincides with the Triassic-Jurassic

boundary (TJB; Schoene et al., 2010; Blackburn et al., 2013; Davies et al., 2017; Fig. 1). CAMP volcanism is envisaged to have released vast quantities of CO_2, SO_2 and toxic metals such as mercury, triggering abrupt climate fluctuations, marine anoxia and acidification, in turn causing widespread disruption to biogeochemical cycles (McElwain et al., 1999; Schaller et al., 2011, 2012; Greene et al., 2012a; Percival et al., 2017; Fujisaki et al., 2020; Li et al., 2022). Stratigraphic records reveal several negative carbon isotope excursions (CIEs) and mercury anomalies that have been linked to volcanic pulses and extinction losses (e.g. Ruhl et al., 2011; Lindström et al., 2019). However, challenges remain in disentangling the relative contributions of volcanism, subsequent environmental feedbacks (e.g., marine anoxia, wildfires), and other potential causes such as bolide impacts or sea-level changes (Olsen et al., 2002; Whiteside et al., 2010; Lindström et al., 2021). In recent decades, numerous multi-proxy studies have evaluated how these different factors interacted and contributed to the ETME (e.g., McElwain et al., 1999; Beerling and Berner, 2002; Hautmann et al., 2008; Bachan and Payne, 2016; Fox et al., 2020, 2022b; Li et al., 2022; Bond et al., 2023). Despite these efforts, the primary kill mechanisms driving the ETME remains unclear.

Here, we review extinction patterns of the ETME across marine and terrestrial ecosystems, the timing and characteristics of the CAMP, and the evidence linking these phenomena with environmental changes. In doing so, we resolve questions regarding the cascading environmental drivers of this major extinction crisis.

2 Extinction magnitudes and patterns

2.1 Terrestrial extinction

Terrestrial tetrapods experienced a dramatic turnover during the Triassic–Jurassic transition (e.g. Olsen et al., 2002; Toljagic and Butler, 2013; Pieńkowski et al., 2014). Some suggest the principal turnover started in the Late Triassic (e.g. Benton, 1993; Lucas et al., 2011), while others opt for a more rapid turnover around the TJB (Olsen et al., 2002). The intra- or end-Rhaetian extinction also affected terrestrial aquatic vertebrates (Hallam, 2002). Benton (1993) reported that by the end of the Rhaetian, 10 reptile families had become extinct, while 12 survived. Plant communities also experienced disruption across the TJB, but relatively few taxa suffered extinction (McElwain et al., 1999, 2009; Barbacka et al., 2017). Generally, Rhaetian and Early Jurassic floras are taxonomically very similar and have traditionally been grouped as 'Rhaetoliassic floras' (Hallam, 2002). Studies of East Greenland flora reveal an abrupt collapse in Late Triassic plant diversity that coincided with rising atmospheric CO_2 levels and global warming (McElwain et al., 1999, 2009). Similarly, palynological records across Europe record major disruptions in plant communities. Rhaetian tree pollen taxa such as *Ovalipollis*, *Rhaetipollis*, *Ricciisporites* and *Classopollis* temporarily disappear and total pollen abundance sharply declines whilst fern and horsetail spores become abundant during the ETME interval (van de Schootbrugge et al., 2009, 2015). The strata between the two marine extinction phases are dominated by fern spores (Wignall and Atkinson, 2020), whilst there was a resurgence of *Classopollis*-producing conifers following the second phase of extinction (Bonis et al., 2010a; Bos et al., 2023).

2.2 Marine extinction

The ETME is well-documented in marine sections where marine reptiles, including thalattosaurs, and nonparvipelvian ichthyosaurs disappeared (Benson and Butler, 2011). In contrast, other marine vertebrates such as fishes did not experience an extinction crisis (McCune and Schaeffer, 1986; Friedman and Sallan, 2012). The ETME led to the extinction of conodonts, devastated corals, sphinctozoan sponges and ammonoids, while also severely affecting other marine invertebrate taxa such as brachiopods and bivalves (Deng et al., 2005; Hautmann, 2012).

2.2.1 Ammonites

Across the Triassic–Jurassic transition, 17 ammonoid families, including the dominant Ceratitina, went extinct. The Choristoceratidae briefly persisted into the Hettangian, while only the Phylloceratina survived and diversified in the Jurassic (Guex et al., 2004; Hillebrandt and Krystyn, 2009; Hautmann, 2012). However, ammonites were generally uncommon in the Rhaetian, with low diversity and richness, and the markedly elevated extinction rates beginning in the middle or late Norian, culminating with their final demise during the ETME (Hallam, 2002).

2.2.2 Bivalves and brachiopods

Marine bivalves are one of the best-studied groups across the TJB. They experienced high extinction magnitudes at both genus and species levels but were relatively unaffected at family level. Losses reached 42% of genera and 92% of species in British successions and in the Northern Calcareous Alps (Hallam, 1981, 2002;

133 Hallam and Wignall, 1997; Hautmann, 2012), although only two families out of 52
134 became extinct (Hallam, 2002). McRoberts and Newton (1995) recognized a selective
135 extinction pattern among end-Triassic European bivalves, with infaunal taxa suffering
136 preferentially in comparison to epifaunal taxa. However, Hallam and Wignall (1997)
137 argued that the survival of species was more likely favored by widespread geographic
138 distribution rather than an epifaunal lifestyle. Notably, larger bivalves faced a higher
139 risk of extinction, and most surviving bivalves are relatively small in size (Hallam, 2002;
140 Deng et al., 2005; Atkinson and Wignall, 2020). Hautmann et al. (2008) proposed that
141 differences in shell mineralogy influenced the extinction pattern, as infaunal bivalves
142 are exclusively aragonitic, whereas epifaunal forms often possess calcitic outer layers.
143 However, the analysis of Ros et al. (2011) did not find any preferential infaunal loss;
144 instead, deeper infaunal burrowers survived better than shallower burrowers.

145 Significant changes occurred in brachiopod faunas across the Triassic–Jurassic
146 transition. Globally, five of 19 families became extinct, and in the Alpine-Carpathian
147 region only five of 13 genera extend into the Jurassic (Pearson, 1997). Articulated
148 brachiopods suffered catastrophic declines in that Alpine-Carpathian region, with 71%
149 generic losses (Hautmann, 2012). Like bivalves, larger brachiopods were less likely to
150 survive the ETME, and there is a predominance of smaller forms in the extinction
151 aftermath (Hallam, 2002; Deng et al., 2005).

152 *2.2.3 Conodonts*

153 Conodonts experienced high extinction magnitudes throughout the Triassic, with
154 peak losses occurring at the end of the Norian with the result that conodont diversity

155 was low in the Rhaetian (De Renzi et al., 1996; Tanner et al., 2004). Subsequently,
156 conodonts suffered their final extinction at the TJB. Du et al. (2020) integrated
157 information about the last occurrences of conodont taxa and major CIEs from different
158 areas and depositional environments and suggested that the final extinction of
159 conodonts was asynchronous. In many successions, conodonts disappear near the initial
160 CIE (corresponding to the first extinction phase) whilst other species survived the first
161 extinction phase and persisted longer in mid-Panthalassa (e.g. the Inuyama area; Du et
162 al., 2020).

163 *2.2.4 Reef building taxa*

164 The ETME witnessed the global collapse of reef ecosystems (Stanley, 1988;
165 Bernecker, 2005; Fig. 2). Scleractinian corals and sphinctozoan sponges, the dominant
166 Triassic reef builders, suffered catastrophic declines, with genus-level extinctions
167 reaching 96% (74/77 coral genera) and 91% (53/58 sponge genera), respectively (Flügel,
168 2002). Calcareous demosponges (sphinctozooids) were also severely affected, with
169 only 2 out of 18 families surviving the Rhaetian (Rigby et al., 1993), as were
170 spongiomorph hydrozoans that disappeared at the end of the Triassic (Hallam, 2002).
171 Reefs re-established during the early Hettangian (e.g., Stanley, 2006), but they were
172 generally small and latitudinally concentrated at around 30°N (Kiessling et al., 2009;
173 Lathuiliere and Marchal, 2009).

174 *2.2.5 Radiolarians*

175 Radiolarians experienced significant turnover during the Triassic–Jurassic
176 transition (Carter, 1993; O'Dogherty et al., 2010; Kocsis et al., 2014), with nearly 20

177 genera and over 130 species disappearing at the end of the Triassic in Japanese and
178 Canadian deep-water successions (Carter and Hori, 2005). Radiolarians suffered
179 stepwise extinctions, with a first phase marked by the loss of many taxa and a sharp
180 decline in abundance of most survivors, followed by phases in which additional taxa
181 disappeared alongside the last conodonts prior to the appearance of primitive and small
182 Early Jurassic radiolarians (Hori et al., 2007; Rigo et al., 2018; Wignall and Atkinson,
183 2020).
184
185 **2.3 Extinction horizon and duration**
186 Early studies considered the ETME to be a culmination of a Late Triassic diversity
187 decline, with many ammonoids, radiolarians, and bivalves becoming extinct due to
188 harsh conditions throughout the Rhaetian (Hallam, 2002; Kent et al., 2017; Galbrun et
189 al., 2020). However, other groups, such as radiolarians and reef taxa, thrived during the
190 Rhaetian (O'Dogherty et al., 2010), suggesting that marine environments were not
191 universally stressed at this time. More recent studies suggest a more rapid crisis
192 occurring within <100 kyr, coinciding with the main phases of CAMP activities (e.g.
193 Wotzlaw et al., 2014; Davies et al., 2017), and has been resolved into a two-phased
194 extinction (Wignall and Atkinson 2020). Within western Europe, the first phase of
195 extinction eliminated around half of bivalve and ostracod species coincident with a
196 short-lived, high-amplitude $\delta^{13}C_{org}$ excursion (the so-called initial CIE; Hesselbo et al.,
197 2002). This was followed by a brief recovery in which diversity partially rebounded
198 before being abruptly terminated by a second extinction phase when a third of bivalve

199 species along with the last conodonts disappeared (Wignall and Atkinson, 2020 and
200 references therein). Globally, this two-phase pattern is corroborated by evidence from
201 multiple regions: all 14 species of brachiopods, and 62% of 39 ostracod species suffered
202 extinction in the Austrian Kössen Basin during the first phase (Hillebrandt et al., 2013).
203 Phased extinction patterns are also recorded in radiolarian faunas in Japan and Canada
204 (e.g. Carter and Hori, 2005; Hori et al., 2007).
205
206 **3. Driving mechanisms**
207 **3.1 Extraterrestrial impact**
208 It has been suggested that the ETME resulted from an extraterrestrial bolide impact
209 (Bice et al., 1992; Olsen et al., 2002). Evidence includes an iridium (Ir) anomaly
210 peaking at 0.285 ppt in the Newark Basin, co-occurring with fern spore spikes, within
211 a white clay layer. The spike is interpreted to record ecological recovery akin to the
212 fern-dominated recovery after the K-Pg crisis (Olsen et al., 2002). Additional support
213 for impact derives from the presence of shocked quartz grains in three distinct layers at
214 the TJB in Italy's Northern Apennines, suggestive of multiple impacts (Bice et al., 1992).
215 In addition, a "seismite" layer in the Cotham Member, southern England lies a few
216 metres below the first appearance of Jurassic ammonites and has been linked to a bolide
217 impact (Simms, 2003).
218 However, the impact hypothesis suffers significant chronological and stratigraphic
219 inconsistencies. High-precision geochronology demonstrates that potential TJB impact
220 structures, like Manicouagan (~214 Ma; Hodych and Dunning, 1992) and Rochechouart

(~207 Ma; Cohen et al., 2017), formed millions of years before the ETME (~201 Ma). The Ir anomaly of Olsen et al. (2002) is more than an order of magnitude smaller than examples recorded at the K-Pg boundary (Pálfy and Kocsis, 2014), and has not been replicated in other sections. The "seismites" of the Cotham Member occur at several layers in the Cotham Member and are probably attributed to the onset of the CAMP (Hallam and Wignall, 2004; Wignall and Bond, 2008; Lindström et al., 2015).

3.2 CAMP volcanism

3.2.1 The formation, characteristics and age of the CAMP

The transition from the Triassic to Jurassic was accompanied by major tectonic and magmatic events linked to the breakup of central Pangea (Marzoli et al., 1999, 2018; Pálfy et al., 2007; Pálfy and Kocsis, 2014; Peace et al., 2020). Intense rifting began to fragment the supercontinent, ultimately leading to the opening of the central Atlantic (Marzoli et al., 1999). The CAMP was emplaced during the initiation of this rifting phase (Peace et al., 2020). Volcanic activity likely began in the late Rhaetian with the emplacement of sills and dykes (Ruhl and Kürschner, 2011), followed by extensive extrusive volcanism across what is now South America, North America, northwest Africa, and southwest Europe (Marzoli et al., 1999; Pálfy and Kocsis, 2014; Fig. 1). Peak volcanism, dating to around 201 Ma, spanned less than a million years and closely coincided with the ETME which occurred prior to 201.51±0.15 Ma (Schoene et al., 2010; Wotzlaw et al., 2014; Marzoli et al., 2011; Blackburn et al., 2013; Davies et al., 2017), although later volcanic pulses occurred during the Sinemurian (Marzoli et al.,

243 2018). Most U-Pb geochronological data indicate that CAMP magmatism occurred
244 between ca. 201.6 and 201.0 Ma; notably, the oldest measured age obtained from
245 Guinea (NW Africa; 201.635 ± 0.029 Ma) closely precedes the marine ETME interval
246 (Schoene et al., 2010; Wotzlaw et al., 2014; Davies et al., 2017; Lindström et al., 2021).
247 Well preserved lava flows are seen in Morocco, Canada, the USA, and Brazil. The
248 original volume of both intrusive and extrusive components is estimated to be $2–4\times10^6$
249 km^3 (McHone, 2003; Marzoli et al., 2018; Lindström et al., 2021; Fig. 1).

250 CAMP activities have long been considered as the ultimate driver of the ETME
251 (e.g. Marzoli et al., 1999, 2018; Wignall, 2001; Pálfy, 2003; Whiteside et al., 2007;
252 Schoene et al., 2010; Blackburn et al., 2013; Percival et al., 2017; Panfili et al., 2019;
253 Kovács et al., 2020; Lindström et al., 2021; Shen et al., 2022a, b). The emplacement of
254 mafic sills into organic-rich sedimentary basins, such as the Amazon Basin, likely
255 triggered the rapid release of isotopically light carbon and sulfur through contact
256 metamorphism of organic- and volatile-rich sediment (Davies et al., 2017).

257 *3.2.2 Mercury as a proxy for CAMP activity*

258 Mercury (Hg) is a volatile heavy metal emitted during volcanic activity with a
259 short atmospheric residence time (~1 year), enabling global dispersion and Hg-
260 enrichment in marine and terrestrial sediments (Lyman et al., 2020). Such signals are
261 often tracked using Hg concentrations normalized to total organic carbon (Hg/TOC;
262 Percival et al., 2017; Grasby et al., 2019; Shen et al., 2019; Yager et al., 2021).
263 Significant sedimentary Hg enrichments and elevated Hg/TOC have been documented
264 during the ETME interval across diverse depositional settings around the world,

ranging from pelagic open ocean, marine shelf, epicontinental sea, terrestrial, and lacustrine sections, attesting to the global distribution of volcanogenic Hg (Percival et al., 2017; Yager et al., 2021; Shen et al., 2022a). These Hg/TOC anomalies are associated with the ETME, with the first Hg peak seen at the first extinction level (Fig. 3; Percival et al., 2017). Furthermore, additional Hg/TOC peaks in multiple sections (e.g. Kuhjoch, Ferguson Hill, Arroyo Malo, and New York Canyon) point to a pulsed CAMP history, implying there were at least two discrete episodes of volcanic activity occurring over ~200 kyr within the ETME interval (Percival et al., 2017).

In addition, mass-independent fractionation (MIF) of mercury isotopes, especially odd-isotopes (e.g., Δ^{199}Hg), has been proven to be a promising tool for tracing Hg sources in sedimentary records (e.g. Blum et al., 2014; Lyman et al., 2020; Shen et al., 2022a). Volcanic emissions release gaseous elemental mercury (Hg^0) with negligible MIF ($\Delta^{199}Hg \approx 0‰$), while photochemical reactions during atmospheric transport would oxidise Hg^0 and form more reactive Hg species with higher Δ^{199}Hg values (Thibodeau and Bergquist, 2017; Bergquist, 2017). Terrestrial vegetation predominantly assimilates atmospheric Hg^0, leading to soils and biomass with negative Δ^{199}Hg values due to the preferential uptake of lighter isotopes, while pelagic marine sediments mainly accumulate oxidised Hg species with higher Δ^{199}Hg values (Demers et al., 2013; Thibodeau and Bergquist, 2017; Zhou et al., 2021).

The Δ^{199}Hg records across the Triassic–Jurassic transition exhibit contrasting signatures in different settings. In the terrestrial Qilixia and Haojiagou sections of western China, Δ^{199}Hg shifts positively towards volcanic Δ^{199}Hg values (+0.02 ±

0.06‰; Fig. 3) near the ETME horizon, implying an enhanced atmospheric flux of volcanogenic Hg (Shen et al., 2022b). However, marine Δ^{199}Hg profiles show various excursion patterns in different sedimentary settings. Analogous to the Haojiagou section, the shallow-marine succession at St. Audrie's Bay (SW England) exhibits negative background Δ^{199}Hg values (−0.4 to −0.2‰), but records a positive excursion towards volcanic values (Δ^{199}Hg ≈ 0‰; vertical shaded bands in Fig. 3) synchronous with Hg/TOC peaks near the first phase of the ETME (Yager et al., 2021). These background Δ^{199}Hg values suggest a strong influence of continental inputs, whereas the Δ^{199}Hg increase towards volcanic values reflects a rapid release of CAMP-derived Hg, which overwhelmed the surface reservoirs and exhibits negligible MIF (Yager et al., 2021; Shen et al., 2022a). The Δ^{199}Hg values in New York Canyon (USA) shelf section are close to volcanic source signal, with no significant excursions during the Hg/TOC enrichment interval (Thibodeau et al., 2016), although the persistence of near-zero Δ^{199}Hg values may reflect mixing of atmospheric (positive MIF) and terrestrial (negative MIF) Hg sources (Shen et al., 2022a). In contrast, the deep marine Levanto and Katsuyama sections exhibit positive background Δ^{199}Hg values indicative of substantial atmospheric deposition, along with a pronounced negative excursion (up to −0.2‰) coinciding with Hg spikes (Fig. 3; Yager et al., 2021; Shen et al., 2022a). This negative excursion has been attributed to the thermal release of low-MIF Hg from organic-rich strata heated by magmatic intrusions (Shen et al., 2022a).

In conclusion, sedimentary Hg proxies (Hg/TOC and Δ^{199}Hg) provide compelling evidence linking CAMP volcanism to the ETME. Globally distributed Hg/TOC peaks

coinciding with the ETME level and pulsed CAMP phases, coupled with sedimentary setting-dependent Δ^{199}Hg excursions, strongly implicate volcanogenic Hg release as the primary driver of mercury cycle perturbations.

4. Biogeochemical perturbations and an environmental crisis

CAMP volcanism is postulated to have caused a cascade of biogeochemical disruptions and environmental effects through coupled volcanic outgassing and contact metamorphism (caused by magmatic intrusions into organic-rich host rocks), inputting CO_2, CH_4, SO_2, halogens (such as Cl, F, Br and halocarbons) and metals (such as Hg and Cu) to the atmosphere. The potential kill mechanisms include (but are not limited to) rapid global warming, marine stratification and anoxia, ocean acidification, nutrient limitation, acid rain and wildfires (Fig. 4), all of which may have contributed to the ecological crisis associated with the ETME.

4.1 Global warming, carbon cycle perturbations, and enhanced continental weathering

Among the main volcanic gases, greenhouse gases (e.g. CO_2 and CH_4) resulting from CAMP volcanism would have driven long-term warming, as seen in both palaeoproxy records and modelling results (McElwain et al., 1999; Korte et al., 2009; Ruhl et al., 2011; Steinthorsdottir et al., 2011; Schaller et al., 2011, 2012, 2015; Bachan and Payne, 2016; Landwehrs et al., 2020). The stomatal density data of plants indicate a rapid warming of 3-4°C during the ETME (McElwain et al., 1999; Retallack, 2001;

Beerling and Berner, 2002; Bonis et al., 2010; Steinthorsdottir et al., 2011; Slodownik et al., 2021), and the $\delta^{13}C$ data of soil carbonate and preserved organic matter from paleosols suggest a 1- to 3-fold increase in atmospheric CO_2 levels, rising from 600-1000 ppm in the Late Triassic to 2000-3000 ppm by the Early Jurassic (Schaller et al., 2011, 2012, 2015; Fig. 5B). This is further supported by Earth system model simulations incorporating pulsed CAMP-derived carbon (2,500-7,500 Gt) and sulfur (0-500 Gt) emissions, which reproduced an initial aerosol-driven cooling of up to 8.1 °C (century-scale average) followed by sustained warming of 1.8 to 4.4 °C as CO_2 accumulated in the atmosphere (Landwehrs et al., 2020).

The emplacement of the CAMP profoundly disrupted the global carbon cycle which underwent pronounced perturbations at the Triassic–Jurassic transition, as evidenced by multiple negative excursions in carbon-isotope records (Beerling and Berner, 2002; Hesselbo et al., 2002, 2020; Kuerschner et al., 2007; Ruhl and Kürschner, 2011; Bachan and Payne, 2016; Zaffani et al., 2018). Three principal events are generally named the precursor CIE, initial CIE, and main CIE (Hesselbo et al., 2002; Ruhl et al., 2009, 2011; Bachan and Payne, 2016; Zaffani et al., 2021; Fig. 5A). The precursor CIE, occurring in the late Rhaetian, aligns with early intrusive CAMP activity (probably the Kakoulima intrusive) and predates the ETME by ~100 kyr (Ruhl and Kürschner, 2011; Davis et al., 2017). The initial CIE coincides with the initiation of main CAMP activities and the first ETME phase, while the main CIE marks prolonged carbon cycle instability extending into the Early Jurassic (Deenen et al., 2010). These negative $\delta^{13}C_{org}$ shifts, recorded globally in marine and terrestrial sediments, are

generally considered to derive from the injection of isotopically light carbon into the ocean-atmosphere system, arising both from direct volcanic CO_2 emissions and from methane generated by thermal alteration of organic-rich strata via contact metamorphism during dyke and sill emplacement (Hesselbo et al., 2002; Ruhl et al., 2011; Ruhl and Kürschner, 2011). Additionally, other mechanisms could have led to the destabilization of marine methane hydrates, including rifting and associated sea-level fall that could have depressurized gas-hydrate-bearing sediments or shoaled the thermocline sufficiently to dissociate methane hydrates (Pálfy et al., 2001; Max and Dillon, 2002; Tanner et al., 2004). The combined effects of volcanic CO_2 pulses, thermogenic methane venting, and hydrate dissociation likely generated several episodes of carbon-cycle perturbations. However, these excursions exhibit considerable variability depending on both the type of archive (e.g., bulk organic matter vs. carbonate) and the palaeogeographical setting (van de Schootbrugge et al., 2008; Schobben et al., 2019; Lindström et al., 2021). This variability complicates global stratigraphic correlation and hampers the distinction between $\delta^{13}C$ signals reflecting global carbon-cycle perturbations and those driven by local environmental processes (Schoepfer et al., 2022).

Abrupt increases in atmospheric pCO_2, acid rain, and the reduction of terrestrial vegetation following major CAMP episodes would all have contributed to a substantial intensification in continental weathering and erosion across the ETME interval (Yapp and Poths, 1999; Cohen and Coe, 2007; Kuroda et al., 2010; Kovács et al., 2020; Zhang et al., 2022; Heszler et al., 2024; Wan et al., 2024). The $^{87}Sr/^{86}Sr$ record exhibits a

375 continuous decline from the late Rhaetian to the ETME horizon, followed by a ~300
376 kyr interval of relative stability and a subsequent transient increase in the early
377 Hettangian (Kovács et al., 2020; Heszler et al., 2024; Fig. 5C). The early Rhaetian
378 decreasing trend in $^{87}Sr/^{86}Sr$ has been interpreted to reflect carbonate and evaporite
379 dissolution and mantle-derived Sr influx during the early rifting of Pangea (Kovács et
380 al., 2020; Onoue et al., 2022; Heszler et al., 2024; Fig. 5C). The interval with a flat
381 trend is attributed to the influx of non-radiogenic Sr derived from the weathering of
382 fresh CAMP basalts, temporarily suppressing the radiogenic continental weathering
383 signal (Heszler et al., 2024). The subsequent rise in $^{87}Sr/^{86}Sr$ in the early Hettangian is
384 interpreted as a response to intensified continental weathering driven by elevated
385 atmospheric CO_2 and a reduced input of mantle-derived Sr flux (Heszler et al., 2024).
386 While the record in the shallow marine Kardolína section (Slovakia) shows an abrupt
387 and large increase in $^{87}Sr/^{86}Sr$ between the precursor and initial CIE (Onoue et al., 2022).
388 However, this shift is interpreted as reflecting an enhanced riverine flux of radiogenic
389 Sr flux locally, rather than a global change in the marine Sr isotope reservoir (Heszler
390 et al., 2024). Other proxies, like Fe-Mg-Zn-Cu isotopes, the chemical index of alteration
391 (CIA), and clay mineralogy from terrestrial sections (e.g., the Qilixia and Haojiagou
392 sections in China), also support an intensification of chemical weathering across the
393 TJB in response to CAMP-driven warmer, more humid conditions (Shen et al., 2022b;
394 Xing et al., 2022; Wan et al., 2024). The episodic emissions associated with CAMP
395 volcanism likely stimulated enhanced silicate weathering, which in turn promoted the
396 drawdown of atmospheric pCO_2 on million-year timescales as a negative feedback

mechanism.

4.2 Widespread marine anoxia

Ocean deoxygenation and the expansion of "dead zones" pose significant threats to modern marine ecosystems. Such zones arise from a combination of factors, including increased terrestrial runoff that promotes salinity stratification and eutrophication, ultimately enhancing primary productivity (Murphy et al., 2011). The enhanced flux of organic matter to the seafloor consumes dissolved oxygen in bottom waters, and in the end Triassic, this would have stimulated the development of anoxic conditions and black shale deposition during the initial CIE (Bonis et al., 2010b). Organic-rich black shale deposits, which indicate widespread bottom-water anoxia, occur near the extinction interval in the Lago Negro Basin of southern Italy (Ciarapica, 2007), the Kössen and Eiberg basins in Austria (Hillebrandt et al., 2013), German Basin (van de Schootbrugge et al., 2013), and Canada (Wignall et al., 2007). In the Eiberg Basin, high TOC (up to 14%) black shales in the uppermost Rhaetian formed during the onset of the initial CIE (Ruhl et al., 2009).

The global extent and role of marine anoxia in the initiation of the ETME remain a topic of debate (e.g., Fujisaki et al., 2020; Li et al., 2022; Bond et al., 2023; Singh et al., 2023; Prow-Fleischer et al., 2025; Fig. 6). In the Central European Basin, on the northwestern margin of the Tethys, redox instability may have begun as early as the mid-Rhaetian (Blumenberg et al., 2016). Some sections, such as St. Audrie's Bay in the UK, record strongly anoxic to euxinic conditions during the extinction interval, as

419 evidenced by the presence of green sulfur bacterial biomarkers (e.g., isorenieratene)
420 and small framboidal pyrite populations (Jaraula et al., 2013; Fox et al., 2022b; Li et
421 al., 2022). At the Kuhjoch section in Austria, framboidal pyrite size-frequency analysis
422 suggests that anoxia was restricted to intervals near the initial CIE and the first
423 extinction horizon, and was followed by a return to oxygenated bottom-water
424 conditions immediately prior to the TJB (Li et al., 2022). These framboidal pyrite data
425 closely align with geochemical data from the nearby Kendlbach section (Pálfy & Zajzon,
426 2012). Multiple positive excursions in δ^{98}Mo from the Schandelah-1 (Germany) and
427 Carnduff-2 (Northern Ireland) cores, alongside moderate Mo enrichment, reflect
428 repeated episodes of euxinia in European successions (Bond et al., 2023).

429 On the Tethyan margin, negative uranium isotope excursions across the ETME
430 point to a rapid global expansion of marine anoxia (Jost et al., 2017). Model simulations
431 using the C-P-U framework suggest that seafloor anoxia reached up to 13% post-
432 extinction, with elevated anoxia persisting into the Hettangian (Somlyay et al., 2023).
433 At the Mount Sparagio section in Italy, a significant positive shift in $\delta^{34}S_{CAS}$ indicates
434 intensified pyrite burial under anoxic conditions, likely driven by low marine sulfate
435 levels that favored the expansion of anoxia during rapid warming (He et al., 2020).
436 However, anoxia had not developed everywhere at the time of the TJB; for instance,
437 there is no evidence for anoxia in the TJB record of Tibet (Hallam et al., 2000). In the
438 Panthalassan realm, intermittent euxinic conditions during the extinction interval and
439 in the Early Jurassic are recorded by biomarkers at the Kennecott Point section in
440 western Canada (Kasprak et al., 2015). Corresponding δ^{15}N data and redox-sensitive

441 elements (e.g., U, Mo) suggest suppressed productivity and the expansion of the OMZ
442 during this interval (Schoepfer et al., 2016). These findings support the model proposed
443 by Fujisaki et al. (2020), which posits a vertical expansion of the OMZ during the Late
444 Triassic, extending anoxia into shallow marine settings. Conversely, elevated MnO
445 concentrations and relatively low Mo and U enrichment in mid-Panthalassan sediments
446 indicate well-oxygenated conditions in deep-sea environments during the Triassic–
447 Jurassic transition (Fujisaki et al., 2020).

448 This spatially heterogeneous redox pattern, especially across the western Tethys
449 European epicontinental shelf, highlights the complex nature of marine anoxia during
450 the ETME interval (Li et al., 2022). Simulations using the Community Earth System
451 Model suggest that variations in ocean circulation and hydrological regimes likely
452 contributed to this heterogeneity (Prow-Fleischer et al., 2025). Although the intensity
453 and duration of marine anoxia varied across the Central European Basin, western Tethys,
454 and Panthalassa, oxygen restriction was a recurring feature of the first extinction phase
455 in multiple settings (Fig. 6). Thus, widespread marine anoxia is increasingly recognized
456 as a key factor in the ETME.

457

458 **4.3 Heterogenous nitrogen cycles and N limitation**

459 The end-Triassic marine nitrogen cycle is characterized by pronounced spatial-
460 temporal heterogeneity, reflecting dynamic interactions between redox conditions,
461 productivity shifts, and regional depositional environments (Fig. 7; Li et al., 2025).
462 Panthalassan shelf sections (e.g., Black Bear Ridge and Kennecott Point in western

463 Canada) record a negative $\delta^{15}N$ excursion to near-zero values preceding and during the
464 ETME interval, indicative of nitrogen limitation and cyanobacteria-dominated N_2
465 fixation under expanded OMZs (Sephton et al., 2002; Schoepfer et al., 2016; Li et al.,
466 2025). These trends correlate with biomarker evidence for photic-zone euxinia and
467 reduced primary productivity, suggesting intensified water-column stratification driven
468 by early CAMP-induced thermal gradients (Kasprak et al., 2015; Fujisaki et al., 2020).
469 In contrast, epicontinental basins (e.g., Doniford Bay, Mariental core) maintained
470 higher $\delta^{15}N$ values (> +2‰) through the Rhaetian, reflecting sustained denitrification
471 in suboxic bottom waters alongside episodic productivity pulses (Paris et al., 2010;
472 Richoz et al., 2012). Spatial variability intensified during the ETME interval: intra-
473 platform basins (Kuhjoch) exhibited positive $\delta^{15}N$ shifts (+ 1-3‰) linked to enhanced
474 water-column denitrification under stratified conditions, while shallow shelves
475 (Mariental) showed muted excursions (~1‰) due to frequent mixing (Quan et al., 2008;
476 Luo et al., 2018). This dichotomy highlights depositional controls, where restricted
477 basins amplified isotopic fractionation through prolonged redox gradients, whereas
478 open shelves experienced buffered N cycling. Mid-Panthalassan deep-sea records
479 (Katsuyama) further complicate interpretation of N records by documenting minor
480 negative $\delta^{15}N$ excursions despite euxinic conditions, likely due to ammonium recycling
481 in photic zones dominated by prasinophytes (Fujisaki et al., 2020). Panthalassan shelf
482 sections retained low $\delta^{15}N$ values into the Hettangian, sustained by chemocline shoaling
483 and ammonium upwelling, while Central European Basin sections display
484 heterogeneous trajectories influenced by terrestrial phosphorus inputs and localized

redox fluctuations (Quan et al., 2008; Schoepfer et al., 2016). Nevertheless, no unified model fully explains $\delta^{15}N$ heterogeneity, as terrestrial influences (e.g., Mingolsheim core) and basin-specific redox architectures modulated nitrogen cycle responses at sub-basin scales. These variations point to widespread but spatially heterogeneous nitrogen limitation, driven by factors such as ocean stratification, productivity decline, and the expansion of OMZs (Li et al., 2025). Although post-extinction nutrient input from enhanced continental weathering may have alleviated N limitation in some areas, local redox and depositional conditions continued to dominate nitrogen cycling into the early Hettangian (Li et al., 2025).

4.4 Sulfur cycle perturbations and a low-sulfate end Triassic

Williford et al. (2009) presented a $\delta^{34}S$ record (samples in a mix of organic sulfur compounds and sedimentary sulfides) from across the Triassic–Jurassic transition, revealing a major perturbation in the sulfur cycle that coincided with a significant carbon cycle disturbance following the ETME. Further, the Tethyan Mount Sparagio section (Italy), the Wenquan section (Qiangtang Basin, Tibet), and the Black Bear Ridge section (Canada) all record sharp positive $\delta^{34}S_{CAS}$ excursions across the extinction horizon, indicating transient euxinic conditions and enhanced removal of ^{32}S by H_2S and pyrite burial (He et al. 2020; Tang et al. 2023; Fig. 8). In addition to $\delta^{34}S_{CAS}$ studies, Jaraula et al. (2013) analyzed pyrite sulfur isotopes ($\delta^{34}S_{py}$) at St. Audrie's Bay and observed positive $\delta^{34}S_{py}$ excursions across the TJB, supporting deposition under euxinic conditions, although their resolution through the ETME interval is relatively low. The

$\delta^{34}S_{py}$ records from the Mariental and Mingolsheim cores indicate an initial phase of oxic to dysoxic deposition punctuated by brief episodes of anoxia coincided with elevated pyrite/TOC ratios and the presence of sulfur bacteria biomarkers, followed by the development of persistent euxinic conditions in the Hettangian (Kasprak et al., 2015; Luo et al., 2018; Fig. 8). These positive $\delta^{34}S$ excursions were likely driven by intensified pyrite burial, aligning with the latest Rhaetian loss of Triassic taxa and the intensification of marine anoxia (Williford et al., 2009; He et al., 2020).

In addition, the massive influx of terrigenous sediments following widespread terrestrial vegetation collapse during the ETME likely decoupled sulfate reduction from sulfate resupply, leading to a reduction in seawater sulfate concentrations (Williford et al., 2009). Under non-sulfate limited conditions with high sulfate concentrations ($[SO_4^{2-}] > 2$ mM), bacterial sulfate reduction (BSR) produces isotopic fractionations ranging from 16‰ to 46‰ relative to seawater sulfate, though repeated sulfur redox cycling in modern marine sediments can amplify fractionations up to 70‰ (Canfield and Raiswell, 1999). However, sulfate limitation begins to constrain BSR below concentrations of ~2 mM, and when seawater $[SO_4^{2-}]$ falls below 0.2 mM, isotopic fractionation drops to less than 10‰ (Habicht et al., 2002). Under conditions of high primary productivity and bottom-water anoxia, sulfate reduction may shift from an open system, sustained by continuous diffusion of sulfate, to a closed system where organic carbon exceeded sulfate supply (Fakhraee et al., 2024). In such cases, Rayleigh fractionation occurs, whereby the residual sulfate pool becomes increasingly enriched in ^{34}S, resulting in progressively heavier $\delta^{34}S$ values in the pyrite formed (Strauss, 1997;

529 Fakhraee et al., 2024). Model simulations of the Mount Sparagio $\delta^{34}S_{CAS}$ record suggest
530 that the observed perturbation of the sulfur biogeochemical cycle is best explained by
531 a concomitant decline in seawater sulfate concentrations, with pre-ETME ocean [SO_4^{2-}]
532 below 1 mM and dropping further during the positive $\delta^{34}S$ excursion interval (He et al.,
533 2020). Although marine sulfate deficiency alone may have not directly caused the
534 ETME, the simulations indicate that sulfate scarcity predisposed pre-ETME oceans to
535 anoxia during rapid warming events by enhancing benthic methane flux and thereby
536 increasing bottom-water oxygen demand (He et al., 2020).
537
538 **4.5 Ocean acidification and carbonate system disruptions**
539 The massive CO_2 influx delivered by CAMP is postulated to have driven ocean
540 acidification (Greene et al., 2012a). Modelled thresholds suggest aragonite
541 undersaturation could occur at atmospheric CO_2 levels > 2000 ppm under Late Triassic
542 oceanic conditions (Berner and Beerling, 2007), while calcite undersaturation required
543 more intense acidification due to its lower solubility (Greene et al., 2012a).
544 Atmospheric CO_2 is thought to have risen from 600-1000 ppm to 2000-3000 ppm across
545 the Triassic–Jurassic transition (McElwain et al., 1999; Schaller et al., 2015; Fig. 5B),
546 reaching levels sufficient to cause widespread undersaturation of both carbonate
547 polymorphs. Lithological evidence is consistent with the modeled results, showing a
548 global reduction in carbonate content across TJB sections, manifested as clay-rich
549 intervals (e.g., the Schattwald Beds in Austria, Lilstock Formation in the UK) and the
550 prevalence of diagenetic carbonate (Hesselbo et al., 2004; Črne et al., 2011; Greene et

al., 2012b). This "carbonate gap" coincides with a negative $\delta^{13}C$ excursion (with amplitude of -3‰ to -8.5‰) reflecting massive light carbon input, likely from CAMP volcanism and thermogenic methane release (Beerling and Berner, 2002; Ruhl et al., 2011).

Negative $\delta^{44/40}Ca$ excursions (up to –0.8‰) that coincide with a negative CIE immediately after the main phase of CAMP activity in Tethyan marginal sections (Lombardian basins, Qiangtang Basin, and Austria) have been interpreted as evidence for ocean acidification, and a marked reduction in $CaCO_3$ burial (Jost et al., 2017; Kovács et al., 2022; Chen et al., 2023). However, a high proportion of aragonite over calcite in the original sediment, reflected in high concentrations of Sr, could have contributed substantially to these negative $\delta^{44/40}Ca$ excursions (Jost et al., 2017). A recent boron isotopic analysis of well-preserved fossil oysters from Lavernock Point (UK) reveals a decline in ocean pH of at least 0.29 units (from 8.24 to 7.93) during the main CIE (Trudgill et al., 2025). This interval, within the earliest Jurassic, is after the second mass extinction phase and during the recovery interval of the marine benthos (Atkinson and Wignall, 2019). Trudgill et al. (2025) conclude that acidification "may have delayed ecosystem recovery", but the fossil record indicates otherwise. Furthermore, the reduction of calcareous nannofossils began prior to the ETME and peaked at the first extinction phase (Clémence et al., 2010), whereas the declines in calcareous-walled phytoplankton in favor of organic-walled and agglutinated taxa occurred after the second extinction phase (van de Schootbrugge et al., 2007). Thus, the role of ocean acidification in driving the ETME remains uncertain.

573

574 **4.6 Acid rain and wildfires**

575 Among the volatiles released from large igneous provinces, large scale emissions
576 of halogens (e.g., F, Cl) deplete the ozone layer (Sigurdsson, 1990) and generate acid
577 rain. The amounts of F and Cl released to the atmosphere by CAMP are estimated to
578 have been high enough to cause significant biological harm if emitted over a short time
579 interval (McHone, 2003; Lindström et al., 2021; Fig. 4). Studies have also proposed
580 that SO_2 emissions from CAMP and the resulting acid rain impacted the end-Triassic
581 climate by driving rapid, short-term cooling and by acidifying soils (Guex et al., 2004;
582 van de Schootbrugge et al., 2009). However, the impact of SO_2 emissions remains
583 difficult to evaluate due to its short residence time in the atmosphere (Lindström et al.,
584 2012). Other evidence for CAMP-related high tropospheric SO_2 perturbations at the
585 TJB includes damaged structures in fossil leaves from Greenland (Bacon et al., 2013;
586 Elliot-Kingston et al., 2014; Steinthorsdottir et al., 2018) and soil acidification (van de
587 Schootbrugge et al., 2009). Whilst likely indicating the regional impact of CAMP
588 volcanism, it is unclear if these effects were sufficiently widespread to cause a global
589 terrestrial crisis.

590 There is also evidence for increased wildfire frequency during the ETME (van de
591 Schootbrugge et al., 2015). Polycyclic aromatic hydrocarbons (PAHs) and charcoal
592 layers across the TJB sequences in Germany, Poland, Greenland, and China record
593 significant wildfire episodes and the combustion of organic sediments (van de
594 Schootbrugge et al., 2009; Marynowski and Simoneit, 2009; Williford et al., 2014;

595 Song et al., 2020; Fox et al., 2022a). Spikes in pyrolytic PAHs such as retene and
596 coronene correlate with an increase in charcoal abundance in plant beds across the TJB
597 in east Greenland, indicating biomass burning (Williford et al., 2014). Records from the
598 Sichuan Basin of China also reveal dual PAH peaks linked to wildfire pulses triggered
599 by CAMP volcanism (Song et al., 2020). However, recent study in the southwest UK
600 challenges the universality of wildfire-driven PAH signals, as their PAH profiles lack
601 clear indicators of intensive local biomass burning and instead point to inputs from soil
602 erosion and distal smoke transport (Fox et al., 2022a). These findings underscore how
603 regional variations in ecosystem response to CAMP volcanism can confound global
604 correlations, highlighting the need for more extensive studies to distinguish localized
605 erosion-derived signals from genuine wildfire imprints in extinction-related carbon-
606 cycle perturbations.
607
608 **5. Synergistic links between CAMP volcanism, environmental change and the**
609 **ETME**
610 CAMP volcanism is widely considered to be the ultimate driver of the ETME, as
611 rapid injections of greenhouse (including thermogenic) gases through volcanic
612 outgassing and magmatic intrusions into organic-rich basins triggered abrupt climatic
613 and carbon cycle perturbations (McElwain et al., 1999; McHone, 2003; Capriolo et al.,
614 2020, 2022). These pulsed inputs of volcanogenic CO_2 and methane produced sustained
615 global warming that directly stressed temperature-sensitive taxa and indirectly altered
616 ocean circulation, promoting enhanced stratification. In turn, this promoted the

development of oxygen deficiency in marginal and epicontinental settings, although redox conditions remained spatially heterogeneous with anoxia developing diachronously across different basins (see Li et al., 2022). Ocean acidification has also been proposed as an additional stress linked to CAMP derived CO_2 release (Greene et al., 2012b; Trudgill et al., 2025), but proxies for pH in ancient oceans remain limited. Biogeochemical cycle disruptions, particularly nitrogen limitation indicated by near-zero $\delta^{15}N$ values in multiple locations (e.g., Schoepfer et al., 2016; Li et al., 2025) and sulfur cycle perturbations reflected by positive $\delta^{34}S$ excursions and marine sulfate drawdown (Williford et al., 2009; He et al., 2020) further amplified environmental stress by suppressing nutrient availability, productivity and altering redox stability, thereby compounding the ecological pressure on marine organisms. On land, elevated temperatures combined with volcanic emissions of SO_2 and halogens promoted acid rain and increased wildfire frequency, contributing to the vegetation turnover, floral collapse, and the widespread deforestation recorded by palynological assemblages (Williford et al., 2014; Song et al., 2020; Fox et al., 2022a).

In this framework, CAMP-driven global warming constitutes the primary driver of the biological turnover, with marine anoxia, biogeochemical cycle perturbations, ocean acidification, and other environmental perturbations acted as secondary stressors, forming a synergistic feedback loop that amplified the stresses and their effects during the ETME (Bond and Grasby, 2017; Schoepfer et al., 2022). Sustained warming and acid rain triggered widespread terrestrial deforestation and wildfires, accelerating nutrient and sediment runoff that fueled coastal eutrophication, strengthened water-

column stratification, and in turn expanded shallow-marine anoxia and PZE, consistent with the conditions recorded across European epicontinental sections (Richoz et al., 2012; Beith et al., 2021; Li et al., 2022; Fox et al., 2022b). Concurrent drawdown of seawater sulfate lowered the threshold for the development of euxinia (He et al., 2020), while nitrogen limitation suppressed primary productivity and placed further stress on food webs (Schoepfer et al., 2016). Ocean acidification, although less well constrained, likely contributed to the collapse of aragonite-dominated reef builders and larger bivalves and brachiopods (Greene et al., 2012). Concurrently, elevated metabolic oxygen demand under warmer and lower-O_2 conditions further exacerbated the disproportionate losses amongst these groups (Song et al., 2021; Singh et al., 2023). Thus, the ETME was initiated by CAMP volcanism and amplified by synergistic feedbacks between warming, anoxia, and disrupted biogeochemical cycles, ultimately resetting marine and terrestrial ecosystems on a global scale.

6. Conclusions

High-precision U-Pb dating of CAMP basalts and ash beds and correlation with the ETME shows a clear synchroneity between these phenomena, implying a causal relationship. Sedimentary mercury (Hg/TOC and Δ^{199}Hg) and multiple CIEs recorded in both marine and terrestrial strata provide further evidence for CAMP volcanism and the disturbance to the C cycle. The massive, pulsed CAMP activities initiated a cascade of environmental perturbations, including rapid global warming, marine stratification and anoxia, ocean acidification, nutrient limitation, acid rain and wildfires, which likely

served as direct kill mechanisms driving the ETME. In contrast, evidence in support of any role for bolide impact is lacking.

Rapid increases in CAMP-derived atmospheric pCO_2 drove global warming and intensified chemical weathering, and contributed to terrestrial ecosystem stress and collapse. Atmospheric CO_2 rise (up to 2,000–3,000 ppm) during the Triassic–Jurassic transition likely lowered seawater pH and carbonate saturation states, leading to undersaturation of aragonite and calcite. However, it is unclear if this was a major factor in the extinction losses. Warming-enhanced hydrological cycling and intensified weathering-driven terrigenous fluxes would have promoted marine stratification that culminated in widespread marine anoxia/euxinia. Despite temporal and spatial heterogeneity, evidence for marine deoxygenation is associated with both extinction phases. In addition, nutrient scarcity, such as widespread but heterogeneous nitrogen limitation inferred from $\delta^{15}N$ records likely reduced productivity, and this may have imposed additional stress on marine organisms.

Acknowledgements:

The authors acknowledge funding support from the National Key R&D Program of China (grant number: 2023YFF0804000) and the Natural Science Foundation of China (grant number: 42172032). DPGB acknowledges funding from the Natural Environment Research Council (NERC Grant NE/V001639/1) and Yong Du acknowledges funding from the China Postdoctoral Science Foundation (grant number: 2025T180107).

References:

Allen, B.J., Stubbs, T.L., Benton, M.J., Puttick, M.N., 2019. Archosauromorph extinction selectivity during the Triassic–Jurassic mass extinction. Palaeontology 62, 211–224.

Atkinson, J.W., Wignall, P.B., 2020. Body size trends and recovery amongst bivalves following the end-Triassic mass extinction. Palaeogeogr. Palaeoclimatol. Palaeoecol. 538, 109453.

Atkinson, J.W., Wignall, P.B., 2019. How quick was marine recovery after the end-Triassic mass extinction and what role did anoxia play? Palaeogeogr. Palaeoclimatol. Palaeoecol. 528, 99–119.

Bachan, A., Payne, J.L., 2016. Modelling the impact of pulsed CAMP volcanism on pCO_2 and $\delta^{13}C$ across the Triassic–Jurassic transition. Geol. Mag. 153, 252–270.

Bacon, K.L., Belcher, C.M., Haworth, M., McElwain, J.C., 2013. Increased atmospheric SO_2 detected from changes in leaf physiognomy across the Triassic-Jurassic boundary interval of East Greenland. PLoS One 8, e60614.

Barbacka, M., Pacyna, G., Kocsis, Á.T., Jarzynka, A., Ziaja, J., Bodor, E., 2017. Changes in terrestrial floras at the Triassic-Jurassic Boundary in Europe. Palaeogeogr. Palaeoclimatol. Palaeoecol. 480, 80–93.

Beerling, D.J., Berner, R.A., 2002. Biogeochemical constraints on the Triassic-Jurassic boundary carbon cycle event. Global Biogeochem. Cycles 16.

Beith, S.J., Calum P. Fox, John E. A. Marshall, Jessica H. Whiteside, 2021. Recurring photic zone euxinia in the northwest Tethys impinged end-Triassic extinction recovery. Palaeogeogr. Palaeoclimatol. Palaeoecol. 584, 110680.

Benson, R.B.J., Butler, R.J., 2011. Uncovering the diversification history of marine tetrapods: ecology influences the effect of geological sampling biases. In: McGowan, A.J. and Smith, A.B. (eds) Comparing the geological and fossil records: Implications for biodiversity studies, pp. 191–208. London: Geol. Soc. Spec. Publ. 358

Benton, M.J., 1993. Reptilia. In: Benton, M.J. (Ed.) The fossil record 2. London: Chapman and Hall, pp. 681-716.

Bergquist, B.A., 2017. Mercury, volcanism, and mass extinctions. Proc. Natl. Acad. Sci. 114, 8675–8677.

Bernecker, M., 2005. Late Triassic reefs from the Northwest and South Tethys: distribution, setting, and biotic composition. Facies 51, 442–453.

Berner, R.A., Beerling, D.J., 2007. Volcanic degassing necessary to produce a $CaCO_3$ undersaturated ocean at the Triassic–Jurassic boundary. Palaeogeogr. Palaeoclimatol. Palaeoecol. 244, 368–373.

Bice, D.M., Newton, C.R., McCauley, S., Reiners, P.W., McRoberts, C.A., 1992. Shocked quartz at the Triassic-Jurassic Boundary in Italy. Science 255, 443–446.

Blackburn, T.J., Olsen, P.E., Bowring, S.A., McLean, N.M., Kent, D.V., Puffer, J., McHone, G., Rasbury, E.T., Et-Touhami, M., 2013. Zircon U-Pb geochronology links the end-Triassic extinction with the Central Atlantic Magmatic Province. Science 340, 941–945.

Blum, J.D., Sherman, L.S., Johnson, M.W., 2014. Mercury isotopes in Earth and environmental sciences. Annu. Rev. Earth Planet. Sci. 42, 249–269.

Blumenberg, M., Heunisch, C., Lückge, A., Scheeder, G., Wiese, F., 2016. Photic zone euxinia in the central Rhaetian Sea prior the Triassic-Jurassic boundary. Palaeogeogr. Palaeoclimatol. Palaeoecol. 461, 55–64.

Bond, A.D., Dickson, A.J., Ruhl, M., Bos, R., van de Schootbrugge, B., 2023. Globally limited but severe shallow-shelf euxinia during the end-Triassic extinction. Nat. Geosci. 16, 1181-1187.

Bond, D.P.G., Grasby, S.E., 2017. On the causes of mass extinctions. Palaeogeogr. Palaeoclimatol. Palaeoecol., 478, 3–29.

Bonis, N.R., Van Konijnenburg-Van Cittert, J.H.A., Kürschner, W.M., 2010a. Changing CO_2 conditions during the end-Triassic inferred from stomatal frequency analysis on Lepidopteris ottonis (Goeppert) Schimper and

Ginkgoites taeniatus (Braun) Harris. Palaeogeogr. Palaeoclimatol. Palaeoecol. 295, 146–161.
Bonis, N.R., Ruhl, M., Kürschner, W.M., 2010b. Climate change driven black shale deposition during the end-Triassic in the western Tethys. Palaeogeogr. Palaeoclimatol. Palaeoecol. 290, 151–159.
Bos, R., Lindström, S., van Konijnenburg-van Cittert, H., Hilgen, F., Hollaar, T.P., Aalpoel, H., van der Weijst, C., Sanei, H., Rudra, A., Sluijs, A., van de Schootbrugge, B., 2023. Triassic-Jurassic vegetation response to carbon cycle perturbations and climate change. Global Planet. Change 228, 104211.
Callegaro, S., Marzoli, A., Bertrand, H., Blichert-Toft, J., Reisberg, L., Cavazzini, G., Jourdan, F., Davies, J., Parisio, L., Bouchet, R., Paul, A., Schaltegger, U., Chiaradia, M., 2017. Geochemical constraints provided by the Freetown Layered Complex (Sierra Leone) on the origin of high-Ti tholeiitic CAMP magmas. J. Petrol. 58, 1811–1840.
Callegaro, S., Rapaille, C., Marzoli, A., Bertrand, H., Chiaradia, M., Reisberg, L., Bellieni, G., Martins, L., Madeira, J., Mata, J., Youbi, N., De Min, A., Azevedo, M.R., Bensalah, M.K., 2014. Enriched mantle source for the Central Atlantic magmatic province: new supporting evidence from Southwestern Europe. Lithos 188, 15–32.
Callegaro, S., Marzoli, A., Bertrand, H., Chiaradia, M., Reisberg, L., Meyzen, C., Bellieni, G., Weems, R.E., Merle, R., 2013. Upper and lower crust recycling in the source of CAMP basaltic dykes from southeastern North America. Earth Planet. Sci. Lett. 376, 186–199.
Canfield, D.E., Raiswell, R., 1999, The evolution of the sulfur cycle. Am. J. Sci. 299, 697–723.
Capriolo, M., Mills, B.J.W., Newton, R.J., Dal Corso, J., Dunhill, A.M., Wignall, P.B., Marzoli, A., 2022. Anthropogenic-scale CO_2 degassing from the Central Atlantic Magmatic Province as a driver of the end-Triassic mass extinction. Global Planet. Change 209, 103731.
Capriolo, M., Marzoli, A., Aradi, L.E., Callegaro, S., Dal Corso, J., Newton, R.J., Mills, B.J.W., Wignall, P.B., Bartoli, O., Baker, D.R., Youbi, N., Remusat, L., Spiess, R., Szabó, C., 2020. Deep CO_2 in the end-Triassic Central Atlantic Magmatic Province. Nat. Commun. 11, 1670.
Carter, E.S., Hori, R.S., 2005. Global correlation of the radiolarian faunal change across the Triassic-Jurassic boundary. Can. J. Earth Sci. 42, 777–790.
Carter, E.S., 1993. Biochronology and Paleontology of uppermost Triassic (Rhaetian) radiolarians, Queen Charlotte Islands, British Columbia, Canada. Lausanne, Switzerland, Mem. Geol. 11, 1–176.
Chen, M., Fu, X., Wang, J., Wei, H., Zhang, Q., Mansour, A., 2023. Tethyan ocean acidification triggered the end-Triassic mass extinction: New Ca isotopic constraints from the Qiangtang Basin. Gondwana. Res. 124, 206–217.
Ciarapica, G., 2007. Regional and global changes around the Triassic–Jurassic boundary reflected in the late Norian–Hettangian history of the Apennine basins. Palaeogeogr. Palaeoclimatol. Palaeoecol. 244, 34–51.
Clémence, M.-E., Gardin, S., Bartolini, A., Paris, G., Beaumont, V., Guex, J., 2010. Bentho-planktonic evidence from the Austrian Alps for a decline in sea-surface carbonate production at the end of the Triassic. Swiss J. Geosci. 103, 293–315.
Cohen, B.E., Mark, D.F., Lee, M.R., Simpson, S.L., 2017. A new high-precision $^{40}Ar/^{39}Ar$ age for the Rochechouart impact structure: At least 5 Ma older than the Triassic–Jurassic boundary. Meteoritics & Planetary Science 52, 1600–1611.
Cohen, A.S., Coe, A.L., 2007. The impact of the Central Atlantic Magmatic Province on climate and on the Sr- and Os-isotope evolution of seawater. Palaeogeogr. Palaeoclimatol. Palaeoecol. 244, 374–390.
Črne, A.E., Weissert, H., Goričan, Š., Bernasconi, S.M., 2011. A biocalcification crisis at the Triassic-Jurassic boundary recorded in the Budva Basin (Dinarides, Montenegro). Geol. Soc. Am. Bull. 123, 40–50.
Davies, J., Marzoli, A., Bertrand, H., Youbi, N., Ernesto, M., Schaltegger, U., 2017. End-Triassic mass extinction started by intrusive CAMP activity. Nat. Commun. 8, 15596.

De Renzi, M., Budorov, K., Sudar, M., 1996. The extinction of conodonts -in terms of discrete elements- at the Triassic-Jurassic boundary. Cuad. Geol. Ibérica 20, 347–366.

Deenen, M.H.L., Ruhl, M., Bonis, N.R., Krijgsman, W., Kuerschner, W.M., Reitsma, M., van Bergen, M.J., 2010. A new chronology for the end-Triassic mass extinction. Earth Planet. Sci. Lett. 291, 113–125.

Demers, J.D., Blum, J.D., Zak, D.R., 2013. Mercury isotopes in a forested ecosystem: implications for air-surface exchange dynamics and the global mercury cycle. Glob. Biogeochem. Cycles 27, 222–238.

Deng, S., Lu, Y., Xu, D., 2005. Progress and review of the studies on the end-Triassic mass extinction event. Sci. China Ser. D-Earth Sci. 48, 2049–2060.

Diaz, R. J., Rosenberg, R., 2008. Spreading dead zones and consequences for marine ecosystems. Science 321, 926–9.

Du, Y., Chiari, M., Karádi, V., Nicora, A., Onoue, T., Pálfy, J., Roghi, G., Tomimatsu, Y., Rigo, M., 2020. The asynchronous disappearance of conodonts: New constraints from Triassic-Jurassic boundary sections in the Tethys and Panthalassa. Earth-Sci. Rev. 203, 103176.

Dunhill, A.M., Foster, W.J., Sciberras, J., Twitchett, R.J., Hautmann, M., 2018. Impact of the Late Triassic mass extinction on functional diversity and composition of marine ecosystems. Palaeontology 61, 133–148.

Fakhraee, M., Crockford, P.W., Bauer, K.W., Pasquier, V., Sugiyama, I., Katsev, S., Raven, M.R., Gomes, M., Philippot, P., Crowe, Sean.A., Tarhan, L.G., Lyons, T.W., Planavsky, N., 2024. The history of Earth's sulfur cycle. Nat. Rev. Earth Environ. 6, 106-125.

Flügel, 2002. Triassic reef patterns. Triassic reef patterns, In Kiessling, W., Flügel, E., Golonka, J. (eds): Phanerozoic Reef Patterns. SEPM (Society for Sedimentary Geology) Special Publications 72, 391-464.

Fox, C. P., Whiteside, J.H., Olsen, P.E., Grice, K., 2022a. Flame out! End-Triassic mass extinction polycyclic aromatic hydrocarbons reflect more than just fire. Earth Planet. Sci. Lett. 584, 117418.

Fox, Calum P., Whiteside, J.H., Olsen, P.E., Cui, X., Summons, R.E., Idiz, E., Grice, K., 2022b. Two-pronged kill mechanism at the end-Triassic mass extinction. Geology 50: 448-453.

Fox, C.P., Cui, X., Whiteside, J.H., Olsen, P.E., Summons, R.E., Grice, K., 2020. Molecular and isotopic evidence reveals the end-Triassic carbon isotope excursion is not from massive exogenous light carbon. Proc. Natl. Acad. Sci. 117, 30171–30178.

Friedman, M., Sallan, L.C., 2012. Five hundred million years of extinction and recovery: a phanerozoic survey of large-scale diversity patterns in fishes. Palaeontology 55, 707–742.

Fujisaki, W., Fukami, Y., Matsui, Y., Sato, T., Sawaki, Y., Suzuki, K., 2020. Redox conditions and nitrogen cycling during the Triassic-Jurassic transition: A new perspective from the mid-Panthalassa. Earth-Sci. Rev. 204, 103173.

Galbrun, B., Boulila, S., Krystyn, L., Richoz, S., Gardin, S., Bartolini, A., Maslo, M., 2020. "Short" or "long" Rhaetian? Astronomical calibration of Austrian key sections. Global Planet. Change 192, 103253.

Götz, A.E., Ruckwied, K., Pálfy, J., Haas, J., 2009. Palynological evidence of synchronous changes within the terrestrial and marine realm at the Triassic/Jurassic boundary (Csővár section, Hungary). Rev. Palaeobot. Palynol. 156, 401–409.

Grasby, S.E., Them, T.R., Chen, Z., Yin, R., Ardakani, O.H., 2019. Mercury as a proxy for volcanic emissions in the geologic record. Earth-Sci. Rev. 196, 102880.

Greene, S.E., Martindale, R.C., Ritterbush, K.A., Bottjer, D.J., Corsetti, F.A., Berelson, W.M., 2012a. Recognising ocean acidification in deep time: An evaluation of the evidence for acidification across the Triassic-Jurassic boundary. Earth-Sci. Rev. 113, 72–93.

Greene, S.E., Bottjer, D.J., Corsetti, F.A., Berelson, W.M., Zonneveld, J.-P., 2012b. A subseafloor carbonate factory across the Triassic-Jurassic transition. Geology 40, 1043–1046.

Guex, J., Bartolini, A., Atudorei, V., Taylor, D., 2004. High-resolution ammonite and carbon isotope stratigraphy across the Triassic–Jurassic boundary at New York Canyon (Nevada). Earth Planet. Sci. Lett. 225, 29–41.

Habicht, K.S., Gade, M., Thamdrup, B., Berg, P., and Canfield, D.E., 2002, Calibration of sulfate levels in the Archean Ocean. Science 298, 2372–2374.

Hall, R.L., Pitaru, S., 2003. Carbon and nitrogen isotope disturbances and an end-Norian (Late Triassic) extinction event: Comment and Reply: comment. Geology 31, e24–e25.

Hallam, T., Wignall, P., 2004. Discussion on sea-level change and facies development across potential Triassic–Jurassic boundary horizons, SW Britain. Comment and Reply: comment. J. Geol. Soc. 161, 1053–1056.

Hallam, A., 2002. How catastrophic was the end-Triassic mass extinction? Lethaia 35, 147–157.

Hallam, A., Wignall, P.B., Yin, J., Riding, J.B., 2000. An investigation into possible facies changes across the Triassic–Jurassic boundary in southern Tibet. Sediment. Geol. 137, 101–106.

Hallam, A., Wignall, P.B., 1997. Mass extinctions and their aftermath. Oxford University Press, UK.

Hallam A., 1981. The end-Triassic bivalve extinction event. Palaeogeogr. Palaeoclimatol. Palaeoecol. 35, 1-44.

Hautmann, M., 2012. Extinction: End-Triassic mass extinction, in: eLS.

Hautmann, M., Stiller, F., Huawei, C., Jingeng, S., 2008. Extinction-recovery pattern of level-bottom faunas across the Triassic-Jurassic boundary in Tibet: Implications for potential killing mechanisms. Palaios 23, 711–718.

He, T., Newton, R.J., Wignall, P.B., Reid, S., Dal Corso, J., Takahashi, S., Wu, H., Todaro, S., Di Stefano, P., Randazzo, V., Rigo, M., Dunhill, A.M., 2022a. Shallow ocean oxygen decline during the end-Triassic mass extinction. Global Planet. Change 210, 103770.

He, T., Wignall, P.B., Newton, R.J., Atkinson, J.W., Keeling, J.F.J., Xiong, Y., Poulton, S.W., 2022b. Extensive marine anoxia in the European epicontinental sea during the end-Triassic mass extinction. Global Planet. Change 210, 103771.

He, T.C., Dal Corso, J., Newton, R.J., Wignall, P.B., Mills, B.J.W., Todaro, S., Stefano, P. D., Turner, E.C., Jamieson, R.A., Randazzo, V., Rigo, M., Jones, R.E., Dunhill, A.M., 2020. An enormous sulfur isotope excursion indicates marine anoxia during the end-Triassic mass extinction. Sci. Adv. 6, eabb6704.

Hesselbo, S.P., Korte, C., Ullmann, C.V., Ebbesen, A.L., 2020. Carbon and oxygen isotope records from the southern Eurasian Seaway following the Triassic-Jurassic boundary: Parallel long-term enhanced carbon burial and seawater warming. Earth-Sci. Rev. 203, 103131.

Hesselbo, S.P., Robinson, S.A., Surlyk, F., 2004. Sea-level change and facies development across potential Triassic–Jurassic boundary horizons, SW Britain. J. Geol. Soc. 161, 1053–1056.

Hesselbo, S.P., Robinson, S.A., Surlyk, F., 2002. Terrestrial and marine extinction at the Triassic-Jurassic boundary synchronized with major carbon-cycle perturbation: A link to initiation of massive volcanism. Geology. 30, 251–254.

Heszler, B., Katchinoff, J., Palcsu, L., Horváth, A., Vallner, Z., Kovács, E.B., Planavsky, N., Pálfy, J., 2024. Marine strontium isotope evolution at the Triassic-Jurassic transition links transient changes in continental weathering to volcanism of the Central Atlantic Magmatic Province. Geochem. Geophys. Geosyst. 25, e2024GC011464.

Hillebrandt, A. v, Krystyn, Kürschner, Bonis, N.R., Ruhl, M., Richoz, S., Schobben, M.A.N., Urlichs, M., Bown, P.R., Kment, K., McRoberts, C.A., Simms, M., and Tomãsových, A., 2013. The Global Stratotype Sections and Point (GSSP) for the base of the Jurassic System at Kuhjoch (Karwendel Mountains, Northern Calcareous Alps, Tyrol, Austria). Episodes 36, 162–198.

Hillebrandt, A.v., Krystyn, L., 2009. On the oldest Jurassic ammonites of Europe (Northern Calcareous Alps, Austria) and their global significance: Neues Jahrbuch für Geologie und Paläontologie Abhandlungen, 253, 163-195.

Hodych, J.P., Dunning, G.R., 1992. Did the Manicouagan impact trigger end-of-Triassic mass extinction? Geology 20, 51–54.

Hori, R.S., Fujiki, T., Inoue, E., Kimura, J.-I., 2007. Platinum group element anomalies and bioevents in the Triassic–Jurassic deep-sea sediments of Panthalassa. Palaeogeogr. Palaeoclimatol. Palaeoecol. 244, 391–406.

Huynh, T.T., Poulsen, C.J., 2005. Rising atmospheric CO_2 as a possible trigger for the end-Triassic mass extinction. Palaeogeogr. Palaeoclimatol. Palaeoecol. 217, 223–242.

Ikeda, M., Hori, R.S., Okada, Y., Nakada, R., 2015. Volcanism and deep-ocean acidification across the end-Triassic extinction event. Palaeogeogr. Palaeoclimatol. Palaeoecol. 440, 725–733.

Jaraula, C.M.B., Grice, K., Twitchett, R.J., Böttcher, M.E., LeMetayer, P., Dastidar, A.G., Opazo, L.F., 2013. Elevated pCO_2 leading to Late Triassic extinction, persistent photic zone euxinia, and rising sea levels. Geology 41, 955–958.

Jørgensen, B.B., Findlay, A.J., Pellerin, A., 2019. The biogeochemical sulfur cycle of marine sediments. Front Microbiol. 10, 849.

Jost, A.B., Bachan, A., van de Schootbrugge, B., Brown, S.T., DePaolo, D.J., Payne, J.L., 2017a. Additive effects of acidification and mineralogy on calcium isotopes in Triassic/Jurassic boundary limestones. Geochem. Geophys. Geosyst. 18, 113–124.

Jost, A.B., Bachan, A., van de Schootbrugge, B., Lau, K.V., Weaver, K.L., Maher, K., Payne, J.L., 2017b. Uranium isotope evidence for an expansion of marine anoxia during the end-Triassic extinction. Geochem. Geophys. Geosyst. 18, 3093–3108.

Kasprak, A.H., Sepúlveda, J., Price-Waldman, R., Williford, K.H., Schoepfer, S.D., Haggart, J.W., Ward, P.D., Summons, R.E., Whiteside, J.H., 2015. Episodic photic zone euxinia in the northeastern Panthalassic Ocean during the end-Triassic extinction. Geology 43, 307–310.

Kent, D.V., Olsen, P.E., 2000. Magnetic polarity stratigraphy and paleolatitude of the Triassic–Jurassic Blomidon Formation in the Fundy basin (Canada): implications for early Mesozoic tropical climate gradients. Earth Planet. Sci. Lett. 179, 311–324.

Kent, D.V., Olsen, P.E., Muttoni, G., 2017. Astrochronostratigraphic polarity time scale (APTS) for the Late Triassic and Early Jurassic from continental sediments and correlation with standard marine stages. Earth-Sci. Rev. 166, 153–180.

Kiessling, W., Roniewicz, E., Villier, L., Léonide, P., Struck, U., 2009. An early Hettangian coral reef in southern France: implications for the end-Triassic reef crisis. Palaios 24, 657-671.

Kiessling, W., Aberhan, M., Brenneis, B., Wagner, P.J., 2007. Extinction trajectories of benthic organisms across the Triassic–Jurassic boundary. Palaeogeogr. Palaeoclimatol. Palaeoecol. 244, 201–222.

Kocsis, A.T., Kiessling, W., Pálfy, J., 2014. Radiolarian diversity dynamics through the Triassic and Jurassic: implications for proximate causes of the end-Triassic mass extinction. Paleobiology 40, 625–639.

Korte, C., Hesselbo, S.P., Jenkyns, H.C., Rickaby, R.E.M., Spötl, C., 2009. Palaeoenvironmental significance of carbon- and oxygen-isotope stratigraphy of marine Triassic–Jurassic boundary sections in SW Britain. J. Geol. Soc. 166, 431–445.

Korte, C., Kozur, H.W., 2011. Bio-and chemostratigraphic assessment of carbon isotope records across the Triassic–Jurassic boundary at Csővár quarry (Hungary) and Kendlbachgraben (Austria) and implications for global correlations. Bull. Geol. Soc. Den. 59, 101–115.

Kovács, Z., Demangel, I., Baldermann, A., Hippler, D., Schmitt, A.-D., Gangloff, S., Krystyn, L., Richoz, S., 2022. The calcium isotope ($\delta^{44/40}Ca$) record through environmental changes: Insights from the Late Triassic. Geochem. Geophys. Geosyst. 23, e2022GC010405.

Kovács, E.B., Ruhl, M., Demény, A., Fórizs, I., Hegyi, I., Horváth-Kostka, Z.R., Móricz, F., Vallner, Z., Pálfy, J., 2020a. Mercury anomalies and carbon isotope excursions in the western Tethyan Csővár section support the link between CAMP volcanism and the end-Triassic extinction. Global Planet. Change 194, 103291.

Kovács, Z., Demangel, I., Richoz, S., Hippler, D., Baldermann, A., Krystyn, L., 2020b. New constraints on the evolution of $^{87}Sr/^{86}Sr$ of seawater during the Upper Triassic. Global Planet. Change 192, 103255.

Kuerschner, W.M., Nina R. Bonis, Leopold Krystyn, 2007. Carbon-isotope stratigraphy and palynostratigraphy of the Triassic–Jurassic transition in the Tiefengraben section — Northern Calcareous Alps (Austria). Palaeogeogr. Palaeoclimatol. Palaeoecol. 244, 257-280.

Kuroda, J., Hori, R.S., Suzuki, K., Gröcke, D.R., Ohkouchi, N., 2010. Marine osmium isotope record across the Triassic-Jurassic boundary from a Pacific pelagic site. Geology 38, 1095–1098.

Landwehrs, J.P., Georg Feulner, Matthias Hofmann, Stefan Petri, 2020. Climatic fluctuations modeled for carbon and sulfur emissions from end-Triassic volcanism. Earth Planet. Sci. Lett. 537, 116174.

Larina, E., Bottjer, D.J., Corsetti, F.A., Thibodeau, A.M., Berelson, W.M., West, A.J., Yager, J.A., 2021. Ecosystem change and carbon cycle perturbation preceded the end-Triassic mass extinction. Earth Planet. Sci. Lett. 576, 117180.

Lathuilière, B., Marchal, D., 2009. Extinction, survival and recovery of corals from the Triassic to Middle Jurassic time. Terra Nova 21, 57–66.

Li, J., Song, H., Du, Y., Wignall, P.B., Bond, D.P.G., Grasby, S.E., Song, Haijun, Dal Corso, J., Tian, L., Chu, D., 2025. Spatial and temporal heterogeneity of the marine nitrogen cycle during the end-Triassic mass extinction. Chem. Geol. 682, 122752.

Li, J., Song, H., Tian, L., Bond, D.P.G., Song, Haijun, Du, Y., Zhang, C., Chu, D., Wignall, P.B., Tong, J., 2022. Dynamic ocean redox conditions during the end-Triassic mass extinction: Evidence from pyrite framboids. Global Planet. Change 218.

Lindström, S., Callegaro, S., Davies, J., Tegner, C., Van De Schootbrugge, B., Pedersen, G.K., Youbi, N., Sanei, H., Marzoli, A., 2021. Tracing volcanic emissions from the Central Atlantic Magmatic Province in the sedimentary record. Earth-Sci. Rev. 212, 103444.

Lindström, S., Sanei, H., van de Schootbrugge, B., Pedersen, G.K., Lesher, C.E., Tegner, C., Heunisch, C., Dybkjær, K., Outridge, P.M., 2019. Volcanic mercury and mutagenesis in land plants during the end-Triassic mass extinction. Sci. Adv. 5, eaaw4018.

Lindström, S., Pedersen, G.K., van de Schootbrugge, B., Hansen, K.H., Kuhlmann, N., Thein, J., Johansson, L., Petersen, H.I., Alwmark, C., Dybkjær, K., Weibel, R., Erlström, M., Nielsen, L.H., Oschmann, W., Tegner, C., 2015. Intense and widespread seismicity during the end-Triassic mass extinction due to emplacement of a large igneous province. Geology 43, 387–390.

Lindström, S., van de Schootbrugge, B., Dybkjær, K., Pedersen, G.K., Fiebig, J., Nielsen, L.H., Richoz, S., 2012. No causal link between terrestrial ecosystem change and methane release during the end-Triassic mass extinction. Geology 40, 531–534.

Lucas, S. G., Tanner, L. H., Donohoo-Hurley, L. L., Geissman, J. W., Kozur, H. W., Heckert, A. B., Weems, R. E., 2011. Position of the Triassic–Jurassic boundary and timing of the end-Triassic extinctions on land: Data from the Moenave Formation on the southern Colorado Plateau, USA. Palaeogeogr. Palaeoclimatol. Palaeoecol. 302, 194-205.

Lucas, S.G., Tanner, L.H., 2015. End-Triassic nonmarine biotic events. J. Palaeogeogr. 4, 331–348.

Luo, G., Richoz, S., van de Schootbrugge, B., Algeo, T.J., Xie, S., Ono, S., Summons, R.E., 2018. Multiple sulfur-isotopic evidence for a shallowly stratified ocean following the Triassic-Jurassic boundary mass extinction. Geochim. Cosmochim. Acta 231, 73–87.

Lyman, S.N., Cheng, I., Gratz, L.E., Weiss-Penzias, P., Zhang, L., 2020. An updated review of atmospheric mercury. Sci. Total Environ. 707, 135575.

Mander, L., Twitchett, R.J., Benton, M.J., 2008. Palaeoecology of the Late Triassic extinction event in the SW UK.

J. Geol. Soc. 165, 319-332.

Marynowski, L., Simoneit, B.R.T., 2009. Widespread Upper Triassic to Lower Jurassic wildfire records from Poland: evidence from charcoal and pyrolytic polycyclic aromatic hydrocarbons. Palaios 24, 785–798.

Marzoli, A., Bertrand, H., Youbi, N., Callegaro, S., Merle, R., Reisberg, L., Chiaradia, M., Brownlee, S., Jourdan, F., Zanetti, A., Davies, J.H.F.L., Cuppone, T., Mahmoudi, A., Medina, F., Renne, P.R., Bellieni, G., Crivellari, S., El Hachimi, H., Bensalah, M.K., Meyzen, C.M., Tegner, C., 2019. The Central Atlantic Magmatic Province (CAMP) in Morocco. J. Petrol. 60, 945–996.

Marzoli, A., Callegaro, S., Dal Corso, J., Davies, J.H.F.L., Chiaradia, M., Youbi, N., Bertrand, H., Reisberg, L., Merle, R., Jourdan, F., 2018. The Central Atlantic Magmatic Province (CAMP): A review. In: Tanner, L.H. (Ed.), The Late Triassic world: Earth in a time of transition. Springer International Publishing, Cham, pp. 91–125.

Marzoli, A., Jourdan, F., Puffer, J.H., Cuppone, T., Tanner, L.H., Weems, R.E., Bertrand, H., Cirilli, S., Bellieni, G., De Min, A., 2011. Timing and duration of the Central Atlantic magmatic province in the Newark and Culpeper basins, eastern U.S.A. Lithos 122:175–188.

Marzoli, A., Bertrand, H., Knight, K.B., Cirilli, S., Buratti, N., Vérati, C., Nomade, S., Renne, P.R., Youbi, N., Martini, R., Allenbach, K., Neuwerth, R., Rapaille, C., Zaninetti, L., Bellieni, G., 2004. Synchrony of the Central Atlantic magmatic province and the Triassic-Jurassic boundary climatic and biotic crisis. Geology 32, 973–976.

Marzoli, A., Renne, P.R., Piccirillo, E.M., Ernesto, M., Bellieni, G., Min, A.D., 1999. Extensive 200-million-year-old continental flood basalts of the Central Atlantic Magmatic Province. Science 284, 616–618.

Max, M.D., Dillon, W.P., 2002. Are Proterozoic cap carbonates and isotopic excursions a record of gas hydrate destabilization following Earth's coldest intervals? Geology 30, 762–763.

McCune, A.R., Schaeffer, B., 1986. Triassic and Jurassic fishes: patterns of diversity. In: Padian, K. (Ed.), The Beginning of the Age of Dinosaurs: Faunal Change across the Triassic-Jurassic Boundary. Cambridge: Cambridge University Press, pp. 171–181.

McElwain, J.C., Beerling, D.J., Woodward, F.I., 1999. Fossil plants and global warming at the Triassic-Jurassic Boundary. Science 285, 1386–1390.

McElwain, J.C., Wagner, P.J., Hesselbo, S.P., 2009. Fossil plant relative abundances indicate sudden loss of Late Triassic biodiversity in East Greenland. Science 324, 1554–6.

McHone, G., 2003. Volatile emissions from Central Atlantic Magmatic Province basalts: Mass assumptions and environmental consequences. Am. Geo phys. Union Monograph, 136, 241–254.

McRoberts, C.A., Newton, C.R., 1995. Selective extinction among end-Triassic European bivalves. Geology 23, 102–104.

Merle, R., Marzoli, A., Bertrand, H., Reisberg, L., Verati, C., Zimmermann, C., Chiaradia, M., Bellieni, G., Ernesto, M., 2011. Ar^{40}/Ar^{39} ages and Sr-Nd-Pb-Os geochemistry of CAMP tholeiites from Western Maranhao basin (NE Brazil). Lithos 122, 137–151.

Merle, R., Marzoli, A., Reisberg, L., Bertrand, H., Nemchin, A., Chiaradia, M., Callegaro, S., Jourdan, F., Bellieni, G., Kontak, D., Puffer, J., McHone, J.G., 2014. Sr, Nd, Pb and Os Isotope systematics of CAMP tholeiites from Eastern North America (ENA): Evidence of a subduction-enriched mantle source. J. Petrol 55, 133–180.

Murphy, R. R., Kemp, W. M., and Ball, W. P. 2011. Longterm trends in Chesapeake Bay seasonal hypoxia, stratification, and nutrient loading. Estuaries and Coasts 34, 1293–309.

O'Dogherty, L., Carter, E.S., Gorican, S., Dumitrica, P., 2010. Triassic radiolarian biostratigraphy. In: Lucas, S.G. (Ed.), The Triassic timescale. Geol. Soc. London Spec. Publ. 334. pp. 163–200.

Olsen, P.E., Kent, D.V., Sues, H.-D., Koeberl, C., Huber, H., Montanari, A., Rainforth, E. C., Fowell, S. J., Szajna, M. J., Harttine, B. W., 2002. Ascent of dinosaurs linked to an iridium anomaly at the Triassic-Jurassic Boundary. Science 296, 1305-1307.

Olsen, P.E., Shubin, N.H., Anders, M.H., 1987. New Early Jurassic Tetrapod Assemblages Constrain Triassic-Jurassic Tetrapod Extinction Event. Science 237, 1025-1029.

Onoue, T., Michalík, J., Shirozu, H., Yamashita, M., Yamashita, K., Kusaka, S., Soda, K., 2022. Extreme continental weathering in the northwestern Tethys during the end-Triassic mass extinction. Palaeogeogr. Palaeoclimatol. Palaeoecol. 594.

Pálfy, J., Kocsis, Á.T., 2014. Volcanism of the Central Atlantic magmatic province as the trigger of environmental and biotic changes around the Triassic-Jurassic boundary. In: Keller, G., Kerr, A.C. (Ed.), Volcanism, Impacts, and Mass Extinctions: Causes and Effects. Geol. Soc. Am. Spec. Pap. 505, 245–261.

Pálfy, J., Zajzon, N., 2012. Environmental changes across the Triassic–Jurassic boundary and coeval volcanism inferred from elemental geochemistry and mineralogy in the Kendlbachgraben section (Northern Calcareous Alps, Austria). Earth Planet. Sci. Lett. 335–336, 121–134.

Pálfy, J., Demény, A., Haas, J., Carter, E.S., Görög, Á., Halász, D., Oravecz-Scheffer, A., Hetényi, M., Márton, E., Orchard, M.J., Ozsvárt, P., Vető, I., Zajzon, N., 2007. Triassic–Jurassic boundary events inferred from integrated stratigraphy of the Csővár section, Hungary. Palaeogeogr. Palaeoclimatol. Palaeoecol. 244, 11–33.

Pálfy, J., 2003, Volcanism of the Central Atlantic magmatic province as a potential driving force in the end-Triassic mass extinction, in Hames, W.E., McHone, J.G., Renne, P.R., and Ruppel, C., (Ed.), The Central Atlantic Magmatic Province: Insights from fragments of Pangea. Am. Geophys. Union, Geophys. Monogr. 136, p. 255–267.

Pálfy, J., Demény, A., Haas, J., Hetényi, M., Orchard, M.J., Vető, I., 2001. Carbon isotope anomaly and other geochemical changes at the Triassic-Jurassic boundary from a marine section in Hungary. Geology 29, 1047–1050.

Panfili, G., Cirilli, S., Corso, J.D., Bertrand, H., Medina, F., Youbi, N., Marzoli, A., 2019. New biostratigraphic constraints show rapid emplacement of the Central Atlantic Magmatic Province (CAMP) during the end-Triassic mass extinction interval. Global Planet. Change 172, 60–68.

Paris, G., Beaumont, V., Bartolini, A., Clémence, M.-E., Gardin, S., Page, K., 2010. Nitrogen isotope record of a perturbed paleoecosystem in the aftermath of the end-Triassic crisis, Doniford section, SW England. Geochem. Geophys. Geosyst. 11.

Peace, A.L., Phethean, J.J.J., Franke, D., Foulger, G.R., Schiffer, C., Welford, J.K., McHone, G., Rocchi, S., Schnabel, M., Dor´e, A.G., 2020. A review of Pangaea dispersal and Large Igneous Provinces – In search of a causative mechanism. Earth-Sci. Rev. 206, 102902.

Pearson, D.A.B. 1977: Rhaetian brachiopods of Europe. Denkschriften der naturhistorisches Museum Wien 1, 1–70.

Percival, L.M.E., Ruhl, M., Hesselbo, S.P., Jenkyns, H.C., Mather, T.A., Whiteside, J.H., 2017. Mercury evidence for pulsed volcanism during the end-Triassic mass extinction. Proc. Natl. Acad. Sci. 114, 7929–7934.

Pieńkowski, G., Niedzwiedzki, G., Brański, P., 2014. Climatic reversals related to the Central Atlantic Magmatic Province caused the end-Triassic crisis—evidence from continental strata in Poland. In: Keller, G., Kerr, A. (Ed.), Volcanism, Impacts, and Mass Extinctions: Causes and Effects. Geol. Soc. America Special Paper 505, 263–286.

Prow-Fleischer, A.N., Lu, Z., Blättler, C.L., He, T., Singh, P., Kemeny, P.C., Todes, J.P., Pohl, A., Bhattacharya, T., van de Schootbrugge, B., Wignall, P.B., Todaro, S., Payne, J.L., 2025. Calcium isotopes support spatial redox gradients on the Tethys European margin across the Triassic-Jurassic boundary. Chem. Geol. 673, 122530.

Quan, T.M., van de Schootbrugge, B., Field, M.P., Rosenthal, Y., Falkowski, P.G., 2008. Nitrogen isotope and trace metal analyses from the Mingolsheim core (Germany): Evidence for redox variations across the Triassic-Jurassic boundary. Global Biogeochem. Cycles 22.

Retallack, G.J., 2001. A 300-million-year record of atmospheric carbon dioxide from fossil plant cuticles. Nature

411, 287–290.
Richoz, S., van de Schootbrugge, B., Pross, J., Püttmann, W., Quan, T.M., Lindström, S., Heunisch, C., Fiebig, J., Maquil, R., Schouten, S., Hauzenberger, C.A., Wignall, P.B., 2012. Hydrogen sulphide poisoning of shallow seas following the end-Triassic extinction. Nat. Geosci. 5, 662–667.
Rigby, J.K., Budd, G.E., Wood, R.A., Debrenne, F., 1993. Porifera. In: Benton M.J. (Ed.), The fossil record 2. London: Chapman and Hall, pp. 77-99.
Rigo, M., Mazza, M., Kara´di, V., Nicora, A., 2018. New Upper Triassic conodont biozo nation of the Tethyan Realm. In: Tanner, L.H. (Ed.), The Late Triassic world: Earth in a time of transition. Springer, Berlin, pp. 189–235.
Ros, S., De Renzi, M., Damborenea, S.E., Márquez-Aliaga, A., 2011. Coping between crises: Early Triassic-early Jurassic bivalve diversity dynamics. Palaeogeogr. Palaeoclimatol. Palaeoecol. 311, 184–199.
Ruhl, M., Bonis, N.R., Reichart, G.J., Sinninghe Damste, J.S., Kurschner, W.M., 2011. Atmospheric carbon injection linked to end-Triassic mass extinction. Science 333, 430–4.
Ruhl, M., Kürschner, W.M., 2011. Multiple phases of carbon cycle disturbance from large igneous province formation at the Triassic-Jurassic transition. Geology 39, 431–434.
Ruhl, M., Kürschner, W.M., Krystyn, L., 2009. Triassic–Jurassic organic carbon isotope stratigraphy of key sections in the western Tethys realm (Austria). Earth Planet. Sci. Lett. 281, 169–187.
Ruiz-Martínez, V.C., Torsvik, T.H., van Hinsbergen, D.J., and Gaina, C., 2012, Earth at 200 Ma: Global palaeogeography refined from CAMP palaeomagnetic data. Earth Planet. Sci. Lett., 331, 67–79.
Schaller, M.F., Wright, J.D., Kent, D.V., 2015. A 30 Myr record of Late Triassic atmospheric pCO_2 variation reflects a fundamental control of the carbon cycle by changes in continental weathering. Geol. Soc. Am. Bull. 127, 661–671.
Schaller, M.F., Wright, J.D., Kent, D.V., Olsen, P.E., 2012. Rapid emplacement of the Central Atlantic Magmatic Province as a net sink for CO_2. Earth Planet. Sci. Lett. 323–324, 27–39.
Schaller, M.F., James D. Wright, Dennis V. Kent, 2011. Atmospheric perturbations associated with the Central Atlantic Magmatic Province. Science 331, 1404–1409.
Schobben, M., Gravendyck, J., Mangels, F., Struck, U., Bussert, R., Kürschner, W.M., Korn, D., Sander, P.M., Aberhan, M., 2019. A comparative study of total organic carbon-$\delta^{13}C$ signatures in the Triassic–Jurassic transitional beds of the Central European Basin and western Tethys shelf seas. Newslett. Stratigr. 52, 461–486.
Schoene, B., Guex, J., Bartolini, A., Schaltegger, U., Blackburn, T.J., 2010. Correlating the end-Triassic mass extinction and flood basalt volcanism at the 100 ka level. Geology 38, 387–390.
Schoepfer, S.D., Algeo, T.J., van de Schootbrugge, B., Whiteside, J.H., 2022. The Triassic–Jurassic transition – A review of environmental change at the dawn of modern life. Earth-Sci. Rev. 232.
Schoepfer, S.D., Algeo, T.J., Ward, P.D., Williford, K.H., Haggart, J.W., 2016. Testing the limits in a greenhouse ocean: Did low nitrogen availability limit marine productivity during the end-Triassic mass extinction? Earth Planet. Sci. Lett. 451, 138–148.
Sephton, M.A., Amor, K., Franchi, I.A., Wignall, P.B., Newton, R., Zonneveld, J.-P., 2002. Carbon and nitrogen isotope disturbances and an end-Norian (Late Triassic) extinction event. Geology 30, 1119–1122.
Sepkoski,J. J. Jr., Mass extinction in the Phanerozoic oceans: A review. Geol. Am. Spec. Pap. 1982, 190, 283–289.
Shen, Jun, Yin, R., Algeo, T.J., Svensen, H.H., Schoepfer, S.D., 2022a. Mercury evidence for combustion of organic-rich sediments during the end-Triassic crisis. Nat. Commun. 13, 1307.
Shen, J., Yin, R., Zhang, S., Algeo, T.J., Bottjer, D.J., Yu, J., Xu, G., Penman, D., Wang, Y., Li, L., Shi, X., Planavsky, N.J., Feng, Q., Xie, S., 2022b. Intensified continental chemical weathering and carbon-cycle perturbations linked to volcanism during the Triassic-Jurassic transition. Nat. Commun. 13, 299.
Sigurdsson, H., 1990. Assessment of the atmospheric impact of volcanic eruptions. In: Sharpton, V.L., Ward, P.D.

(Ed.), Global Catastrophes in Earth History, Geol. Soc. Am. Spec. Pap. 247, pp. 99–110.
Simms, M.J., 2003. Uniquely extensive seismite from the latest Triassic of the United Kingdom: Evidence for bolide impact? Geology 31, 557–560.
Singh, P., Lu, W., Lu, Z., Jost, A.B., Lau, K., Bachan, A., van de Schootbrugge, B., Payne, J.L., 2023. Reduction in animal abundance and oxygen availability during and after the end-Triassic mass extinction. Geobiology 21, 175–192.
Slodownik, M., Vajda, V., Steinthorsdottir, M., 2021. Fossil seed fern Lepidopteris ottonis from Sweden records increasing CO_2 concentration during the end-Triassic extinction event. Palaeogeogr. Palaeoclimatol. Palaeoecol. 564, 110157.
Somlyay, A., Palcsu, L., Kiss, G.I., Clarkson, M.O., Kovács, E.B., Vallner, Z., Zajzon, N., Pálfy, J., 2023. Uranium isotope evidence for extensive seafloor anoxia after the end-Triassic mass extinction. Earth Planet. Sci. Lett. 614, 118190.
Song, H., Kemp, D.B., Tian, L., Chu, D., Song, H., Dai, X., 2021. Thresholds of temperature change for mass extinctions. Nat. Commun. 12, 4694.
Song, Y., Algeo, T.J., Wu, W., Luo, G., Lie, L., Wang, Y., Xie, S., 2020. Distribution of pyrolytic PAHs across the Triassic-Jurassic boundary in the Sichuan Basin, southwestern China: Evidence of wildfire outside the Central Atlantic Magmatic Province. Earth-Sci. Rev. 201, 102970.
Spray, J.G., Kelley, S.P., Rowley, D.B., 1998. Evidence for a late Triassic multiple impact event on Earth. Nature 392, 171–173.
Stanley, G.D., 2006. Photosymbiosis and the evolution of Modern Coral Reefs. Science 312, 857–858.
Stanley. G. D., The history of early Mesozoic reef communities: a three-step process. Palaios 1988, 170-183.
Steinthorsdottir, M., Jeram, A.J., McElwain, J.C., 2011. Extremely elevated CO_2 concentrations at the Triassic/Jurassic boundary. Palaeogeogr. Palaeoclimatol. Palaeoecol. 308, 418–432.
Strauss, H., 1997, The isotopic composition of sedimentary sulfur through time. Palaeogeogr. Palaeoclimatol. Palaeoecol. 132, 97–118
Tang, W., Wang, J., Wei, H., Fu, X., Ke, P., 2023. Sulfur isotopic evidence for global marine anoxia and low seawater sulfate concentration during the Late Triassic. J. Asian Earth Sci. 251, 105659.
Tanner, L.H., Lucas, S.G., Chapman, M.G., 2004. Assessing the record and causes of Late Triassic extinctions. Earth-Sci. Rev. 65, 103–139.
Thibodeau, A.M., Bergquist, B.A., 2017. Do mercury isotopes record the signature of massive volcanism in marine sedimentary records? Geology. 45, 95–96.
Thibodeau, A.M., Ritterbush, K., Yager, J.A., West, A.J., Ibarra, Y., Bottjer, D.J., Berelson, W.M., Bergquist, B.A., Corsetti, F.A., 2016. Mercury anomalies and the timing of biotic recovery following the end-Triassic mass extinction. Nat. Commun. 7, 11147.
Toljagic, O., and Butler, R.J., 2013. Triassic-Jurassic mass extinction as a trigger for the Mesozoic radiation of crocodylomorphs. Biol. Lett. 9, 20130095.
Trudgill, M., Rae, J.W.B., Whiteford, R., Adloff, M., Crumpton-Banks, J., Van Mourik, M., Burke, A., Cuperus, M., Corsetti, F., Doherty, D., Gray, W., Greenop, R., Hong, W.-L., Lepland, A., McIntyre, A., Neiroukh, N., Rose, C.V., Ruhl, M., Saunders, D., Siri, M.M.F.R., Steele, R.C.J., Stüeken, E.E., West, A.J., Ziegler, M., Greene, S.E., 2025. Pulses of ocean acidification at the Triassic–Jurassic boundary. Nat. Commun. 16, 1–11.
van de Schootbrugge, B., van der Weijst, C.M.H., Hollaar, T.P., Vecoli, M., Strother, P.K., Kuhlmann, N., Thein, J., Visscher, H., van Konijnenburg-van Cittert, H., Schobben, M.A.N., Sluijs, A., Lindström, S., 2020. Catastrophic soil loss associated with end-Triassic deforestation. Earth-Sci. Rev. 210, 103332.
van de Schootbrugge, B., Wignall, P.B., 2015. A tale of two extinctions: converging end-Permian and end-Triassic

scenarios. Geol. Mag. 153, 332–354.
van de Schootbrugge, B., Bachan, A., Suan, G., Richoz, S., Payne, J.L., Jagt, J., 2013. Microbes, mud and methane: cause and consequence of recurrent Early Jurassic anoxia following the end-Triassic mass extinction. Palaeontology 56, 685–709.
van de Schootbrugge, B., Quan, T.M., Lindström, S., Püttmann, W., Heunisch, C., Pross, J., Fiebig, J., Petschick, R., Röhling, H.G., Richoz, S., Rosenthal, Y., Falkowski, P.G., 2009. Floral changes across the Triassic/Jurassic boundary linked to flood basalt volcanism. Nat. Geosci. 2, 589–594.
van de Schootbrugge, B., Payne, J.L., Tomasovych, A., Pross, J., Fiebig, J., Benbrahim, M., Föllmi, K.B., Quan, T.M., 2008. Carbon cycle perturbation and stabilization in the wake of the Triassic-Jurassic boundary mass-extinction event. Geochem. Geophys. Geosyst. 9, 2007GC001914.
van de Schootbrugge, B., Tremolada, F., Rosenthal, Y., Bailey, T.R., Feist-Burkhardt, S., Brinkhuis, H., Pross, J., Kent, D.V., Falkowski, P.G., 2007. End-Triassic calcification crisis and blooms of organic-walled 'disaster species.' Palaeogeogr. Palaeoclimatol. Palaeoecol. 244, 126–141.
Wan, R., Yuan, C., Liu, S.-A., Fang, L., Shen, J., Wang, X., 2024. Intensified continental weathering and reductive surface runoff during the Triassic–Jurassic transition. Geology 53, 13–17.
Ward, P.D., Haggart, J.W., Carter, E.S., Wilbur, D., Tipper, H.W., Evans, T., 2001. Sudden productivity collapse associated with the Triassic-Jurassic boundary mass extinction. Science 292, 1148–1151.
Weedon, G.P., Jenkyns, H.C., 1999. Cyclostratigraphy and the Early Jurassic timescale: Data from the Belemnite Marls, Dorset, southern England. Geol. Soc. Am. Bull. 111, 1823–1840.
Whiteside, J.H., Olsen, P.E., Eglinton, T., Brookfield, M.E., Sambrotto, R.N., 2010. Compound-specific carbon isotopes from Earth's largest flood basalt eruptions directly linked to the end-Triassic mass extinction. Proc. Natl. Acad. Sci. 107, 6721–5.
Whiteside, J.H., Olsen, P.E., Kent, D.V., Fowell, S.J., Et-Touhami, M., 2007. Synchrony between the Central Atlantic magmatic province and the Triassic–Jurassic mass-extinction event? Palaeogeogr. Palaeoclimatol. Palaeoecol. 244, 345–367.
Wignall, P.B., Atkinson, J.W., 2020. A two-phase end-Triassic mass extinction. Earth-Sci. Rev. 208, 103282.
Wignall, P.B., Bond, D.P.G., 2008. The end-Triassic and Early Jurassic mass extinction records in the British Isles. Proc. Geol. Assoc. 119, 73–84.
Wignall, P.B., Zonneveld, J.P., Newton, R.J., Amor, K., Sephton, M.A., Hartley, S., 2007. The end Triassic mass extinction record of Williston Lake, British Columbia. Palaeogeogr. Palaeoclimatol. Palaeoecol. 253, 385–406.
Wignall, P.B., 2001. Sedimentology of the Triassic-Jurassic boundary beds in Pinhay Bay (Devon, SW England). Proc. Geol. Assoc. 112 (4), 349–360.Williford, K.H., Grice, K., Holman, A., McElwain, J.C., 2014. An organic record of terrestrial ecosystem collapse and recovery at the Triassic–Jurassic boundary in East Greenland. Geochim. Cosmochim. Acta 127, 251–263.
Williford, K.H., Foriel, J., Ward, P.D., Steig, E.J., 2009. Major perturbation in sulfur cycling at the Triassic-Jurassic boundary. Geology 37, 835–838.
Wotzlaw, J.-F., Guex, J., Bartolini, A., Gallet, Y., Krystyn, L., McRoberts, C.A., Taylor, D., Schoene, B., Schaltegger, U., 2014. Towards accurate numerical calibration of the Late Triassic: High-precision U-Pb geochronology constraints on the duration of the Rhaetian. Geology 42, 571–574.
Xing, K.-C., Wang, F., Teng, F.-Z., Xu, W.-L., Li, M., Sun, Y.-W., Yang, D.-B., 2022. High-latitude climatic response across the Triassic-Jurassic boundary recorded by Mg-Cu-Zn isotopes. Chem. Geol. 610, 121085.
Yager, J.A., West, A.J., Thibodeau, A.M., Corsetti, F.A., Rigo, M., Berelson, W.M., Bottjer, D.J., Greene, S.E., Ibarra, Y., Jadoul, F., Ritterbush, K.A., Rollins, N., Rosas, S., Di Stefano, P., Sulca, D., Todaro, S., Wynn, P., Zimmermann, L., Bergquist, B.A., 2021. Mercury contents and isotope ratios from diverse depositional

environments across the Triassic–Jurassic Boundary: Towards a more robust mercury proxy for large igneous province magmatism. Earth-Sci. Rev. 223, 103775.

Yapp, C.J., Poths, H., 1996. Carbon isotopes in continental weathering environments and variations in ancient atmospheric CO_2 pressure. Earth Planet. Sci. Lett. 137, 71–82.

Yin, J., Enay, R., Wan, X., 1999. The first report of the Late Triassic-Early Jurassic passage beds in the Eastern Tethyan Himalaya. Comptes Rendus de l'Académie des Sciences - Series IIA - Earth Planet. Sci. 329, 125–133.

Zaffani, M., Jadoul, F., Rigo, M., 2018. A new Rhaetian $\delta^{13}C_{org}$ record: Carbon cycle disturbances, volcanism, End-Triassic mass Extinction (ETE). Earth-Sci. Rev. 178, 92–104.

Zhang, Xiaoyu, Lv, P., Fang, L., Wang, G., Lu, Y., Deng, S., Yang, H., Fang, Y., Li, H., Zhang, Xinzhi, Sun, Y., Chen, Y., Shi, S., 2022. Biomarker evidence for deforestation across the Triassic-Jurassic boundary in t`he high palaeolatitude Junggar Basin, northwest China. Palaeogeogr. Palaeoclimatol. Palaeoecol. 600, 111074.

Zhou, J., Obrist, D., Dastoor, A., Jiskra, M., Ryjkov, A., 2021. Vegetation uptake of mercury and impacts on global cycling. Nat. Rev. 2, 269–284.

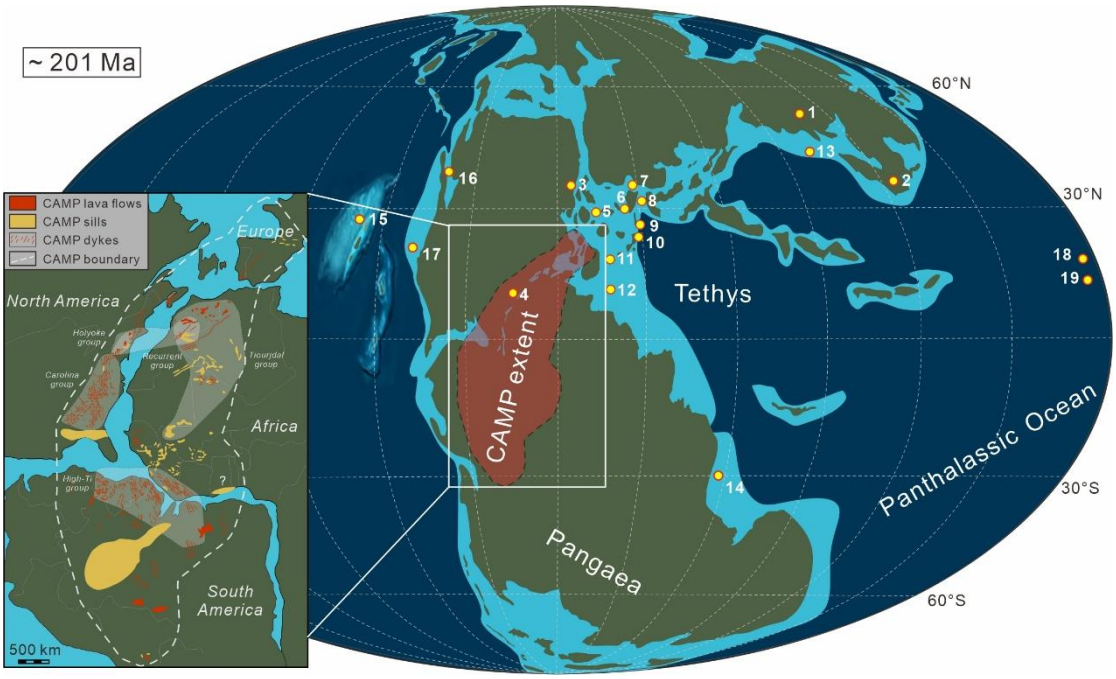

1179

1180 Fig. 1. Palaeogeographic map of Pangea, the extent of CAMP emplacement, and key TJB
1181 successions mentioned in the text (adapted from Schoepfer et al., 2022). The zoomed inset shows
1182 the schematic map of the CAMP on the Pangaean continent (adapted after Marzoli et al., 2018).
1183 Terrestrial sites: (1) Haojiagou section, Junggar Basin, China (Shen et al., 2022b); (2) Qilixia section,
1184 Sichuan Basin, China (Shen et al., 2022b); (3) East Greenland, Greenland (McElwain et al., 1999,
1185 2009); (4) Newark Basin, USA (Marzoli et al., 2004, 2011; Blackburn, 2013). Tethyan sites: (5) St.
1186 Audrie's Bay, UK (Warrington et al., 1994; Hesselbo et al., 2002, 2004); (6) Mingolsheim core,
1187 German basin, Germany (Quan et al., 2008; van de Schootbrugge et al., 2008, 2013); (7) Mariental
1188 core, German basin, Germany (Heunisch et al., 2010; Richoz et al., 2012); (8) Csővár section,
1189 Hungary (Götz et al., 2009; Haas et al., 2010; Kovács et al., 2020); (9) Kuhjoch section, Austria
1190 (GSSP; Ruhl et al., 2009; Bonis et al., 2010; Hillebrandt et al., 2013); (10) Italcementi section, Italy
1191 (Galli et al., 2005, 2007); (11) Lombardy Basin, Hungary (Galli et al., 2005, 2007); (12) Mount
1192 Sparagio section, Italy (Todaro et al., 2017); (13) Wenquan Section, Qiangtang basin, China (Hu et
1193 al, 2020); (14) Germig section, southern Tibet, China (Yin et al., 1999; Hallam et al., 2000).
1194 Panthalassan sites: (15) Kennecott Point, Canada (Ward et al., 2001, 2004; Carter and Orchard,
1195 2007); (16) Williston Lake, British Columbia, Canada (Wignall et al., 2007); (17) New York Canyon,
1196 USA (Guex et al., 2004); (18) Katsuyama section, Japan (Fujisaki et al., 2020); (19) Kurusu section,
1197 Japan (Cater and Hori, 2005; Hori et al., 2007).

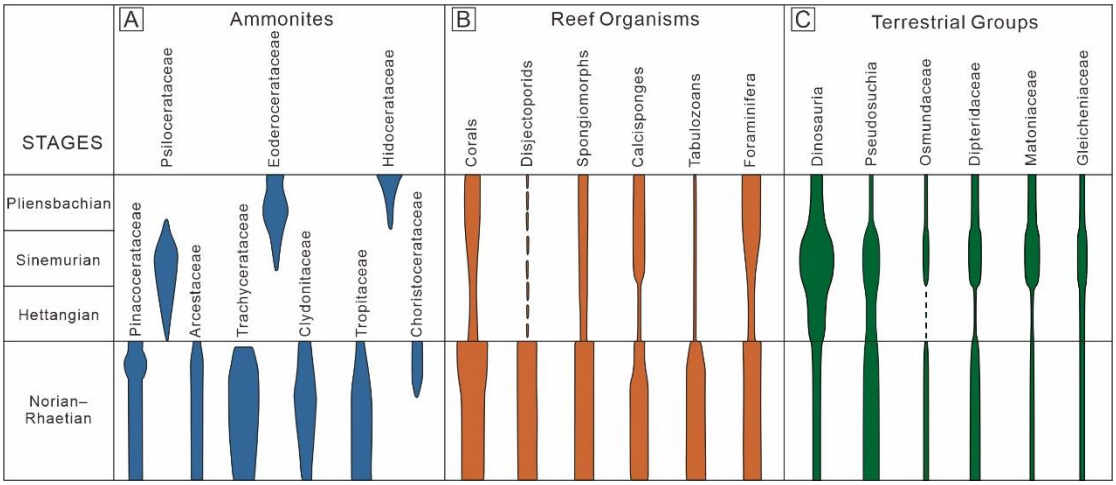

Fig. 2. End-Triassic mass extinction in important marine groups. A, ammonites; and B, reef organisms are modified after Hallam and Wignall (1997). C, selected terrestrial groups, compiled from Paleobiology Database in late February 2026 (https://paleobiodb.org/).

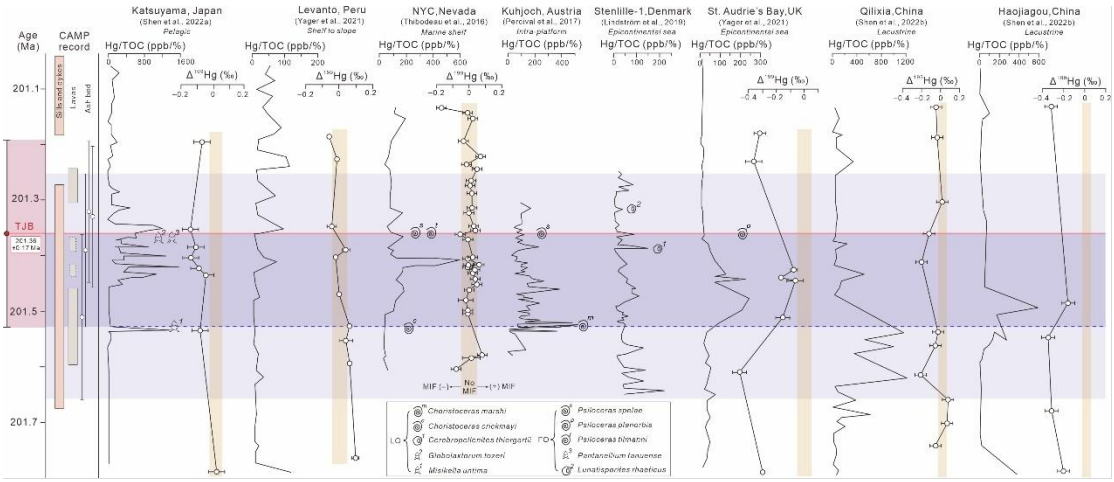

Fig. 3. Correlations of CAMP emplacement records, sedimentary Hg/TOC and Δ^{199}Hg data across various settings, and the ETME interval. CAMP data (sills and dykes, lavas, and ash beds) are based on Lindström et al. (2019). The solid red line marks the TJB, and the dashed blue line denotes the and the onset of the ETME. The ETME interval is shaded purple, with light-purple area indicating its age uncertainties. For the Δ^{199}Hg data, the vertical shaded bands represent the volcanic Δ^{199}Hg endmember (0.02 ± 0.06‰); horizontal bars of the Δ^{199}Hg profiles represent standard deviation (2σ) values. Data sources by setting: Pelagic (Katsuyama, Shen et al., 2022a); shelf to slope (Levanto, Yager et al., 2021); marine shelf (NYC, Thibodeau et al., 2016); intra-platform (Kuhjoch, Percival et al., 2017); epicontinental sea (Stenlille-1, Lindström et al., 2019; St. Audrie's Bay, Yager et al., 2021); lacustrine (Qilixia and Haojiagou, Shen et al., 2022b). NYC, New York Canyon; LO, last occurrence; FO, First Occurrence.

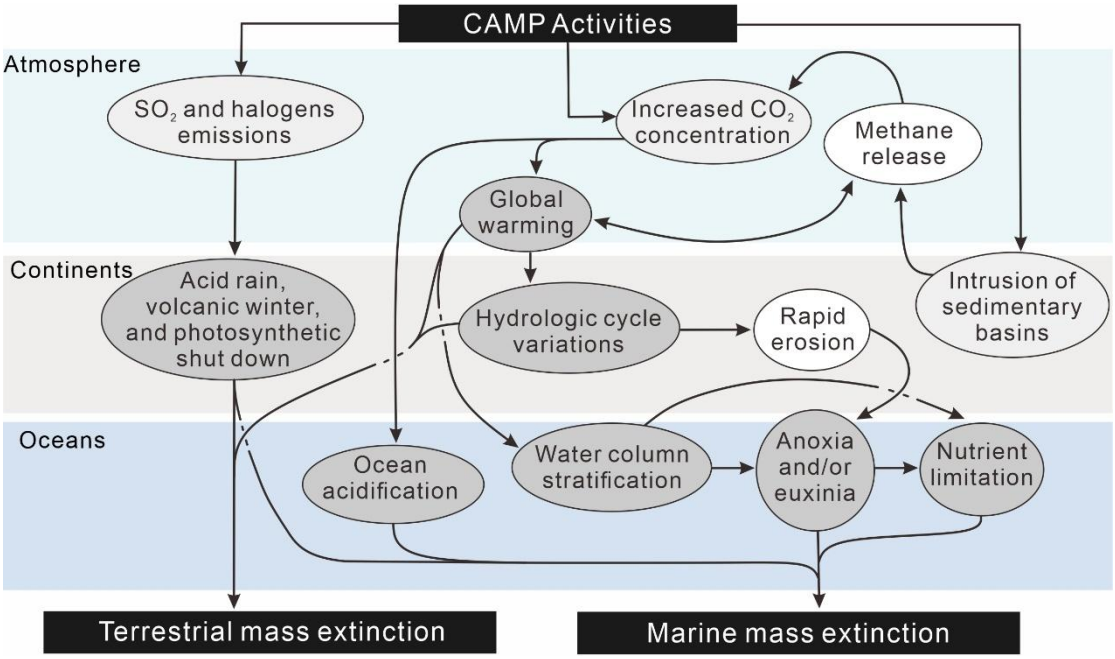

1216

1217 Fig. 4. Proposed cause-and-effect relationships of major changes in the atmosphere, terrestrial
1218 realm, and oceans following the CAMP activities during the ETME. Modified after Bond and
1219 Grasby (2017) and Schoepfer et al. (2022). Light grey ellipses = direct products of volcanism; dark
1220 grey ellipses = proximal kill mechanisms; white ellipses = knock-on effects and isotopic signatures.
1221

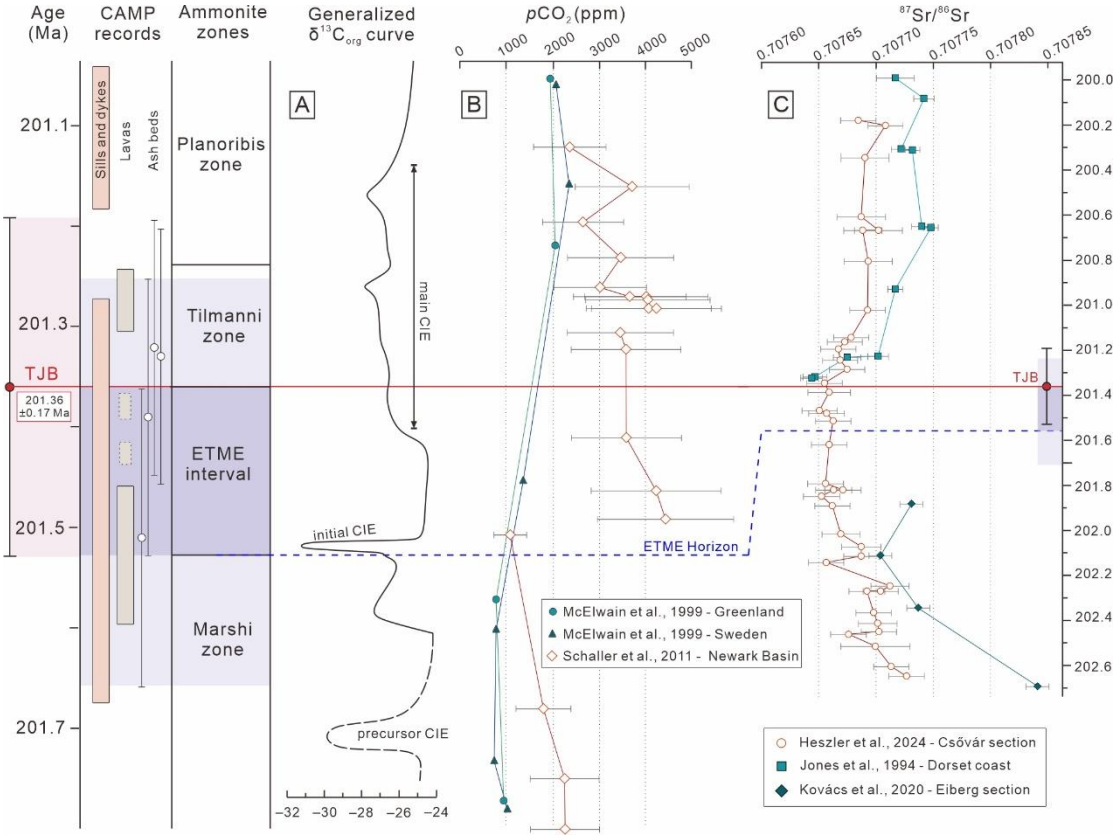

Fig. 5. A. Generalized $\delta^{13}C_{org}$ curve across the ETME interval. B. Simulated pCO_2 by $\delta^{13}C$ data of soil carbonate and preserved organic matter from paleosols (Schaller et al., 2011) and stomatal density data focusing on the ETME interval (McElwain et al., 1999). C. Compilation of $^{87}Sr/^{86}Sr$ data from the TJB. Diamonds: bulk carbonate from Eiberg section, North Calcareous Alps (Kovács et al., 2020); squares: Lyme Regis oysters from Dorset (Jones et al., 1994); circles: bulk carbonate from Csővár section (Heszler et al., 2024). Ages are plotted using correlated floating astrochronological age models or recalculated to the GTS 2020, cited after Heszler et al. (2024). Error bars are 2sd.

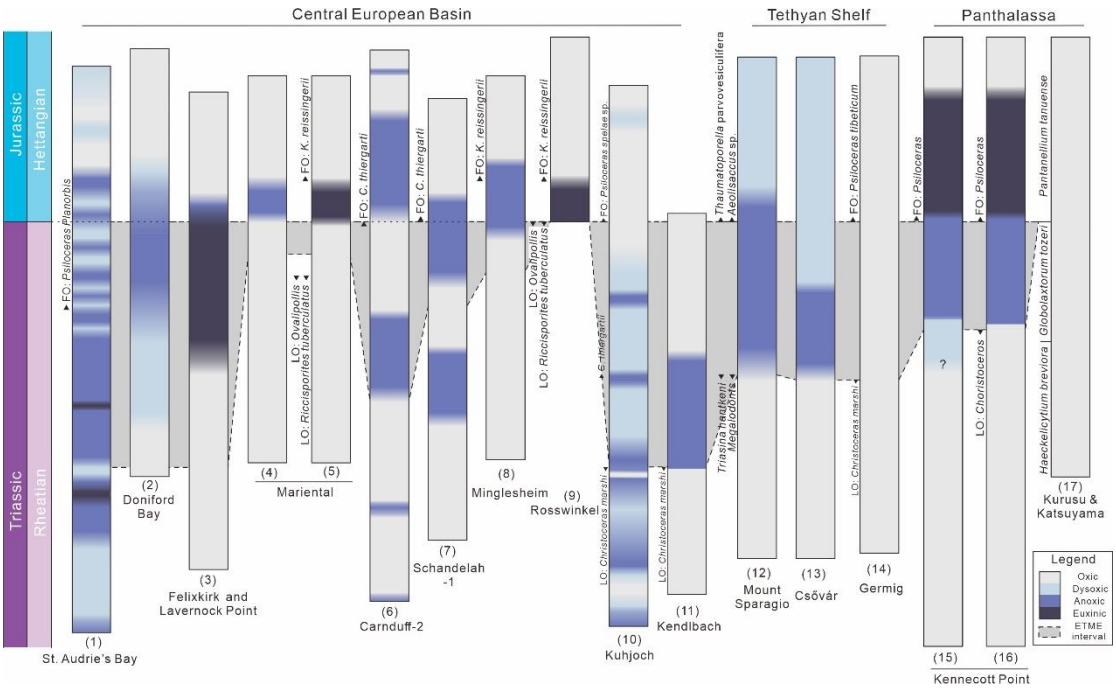

Fig. 6. Global correlation of redox conditions across the Triassic-Jurassic transition (adapted after Li et al., 2022). Sections: 1 = St. Audrie's Bay, UK (Li et al., 2022; pyrite framboids); 2 = Doniford Bay, UK (Paris et al., 2010; $\delta^{15}N$); 3 = Felixkirk and Lavernock Point, UK (Beith et al., 2021; biomarker); 4 = Mariental, Germany (Luo et al., 2018; sulfur isotopes); 5 = Mariental, Germany (Richoz et al., 2012; biomarker); 6 = Canduff-1 core (Bond et al., 2023; Mo isotopes); 7 = Schandelah-1 core (Bond et al., 2023; Mo isotopes); 8 = Minglesheim, Germany (Luo et al., 2018; sulfur isotopes); 9 = Rosswinkel, Luxembourg (Richoz et al., 2012; biomarker); 10 = Kuhjoch, Austria (Li et al., 2022; pyrite framboids); 11 = Kendlbach, Austria (Pálfy and Zajzon., 2012; rare Earth elements); 12 = Mount Sparagio, Italy (He et al., 2020, 2022b; $\delta^{34}S_{CAS}$ and I/(Ca+Mg)); 13 = Csővár section (Somlyay et al., 2023; U isotopes); 14 = Germig sections, China (Hallam et al., 2000; Th/U ratio); 15 = Kennecott Point, Canada (Schoepfer et al., 2016; $\delta^{15}N$); 16 = Kennecott Point, Canada (Kasprak et al., 2015; biomarker); 17 = Kurusu and Katsuyama sections, Japan (Fujisaki et al., 2020; $\delta^{15}N$). Abbreviations: LO: last occurrence; FO: first occurrence. The ETME interval is constrained by the LO of the ammonite *Christoceras marshi* and the FO of *Psiloceras spelae* in the GSSP section at Kuhjoch. Question marks denote probable anoxic/dysoxic conditions.

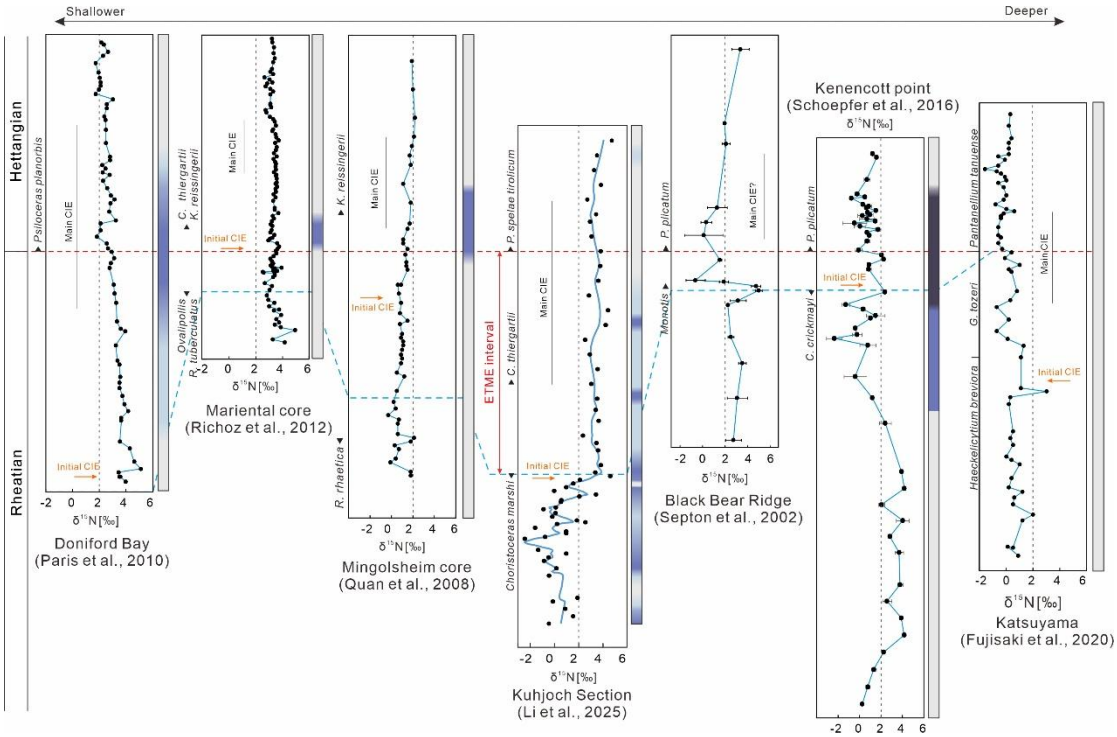

Fig. 7. Compilation of sedimentary $\delta^{15}N$ records (adapted after Li et al., 2025) and related redox variations (citations see Fig. 6) across the Triassic–Jurassic transition. Orange arrows and the vertical bars denote the position the position of initial CIEs and the rough range of main CIEs. Blue and orange dashed lines represent the ETME horizon and the TJB, respectively, with the ETME interval falling between these.

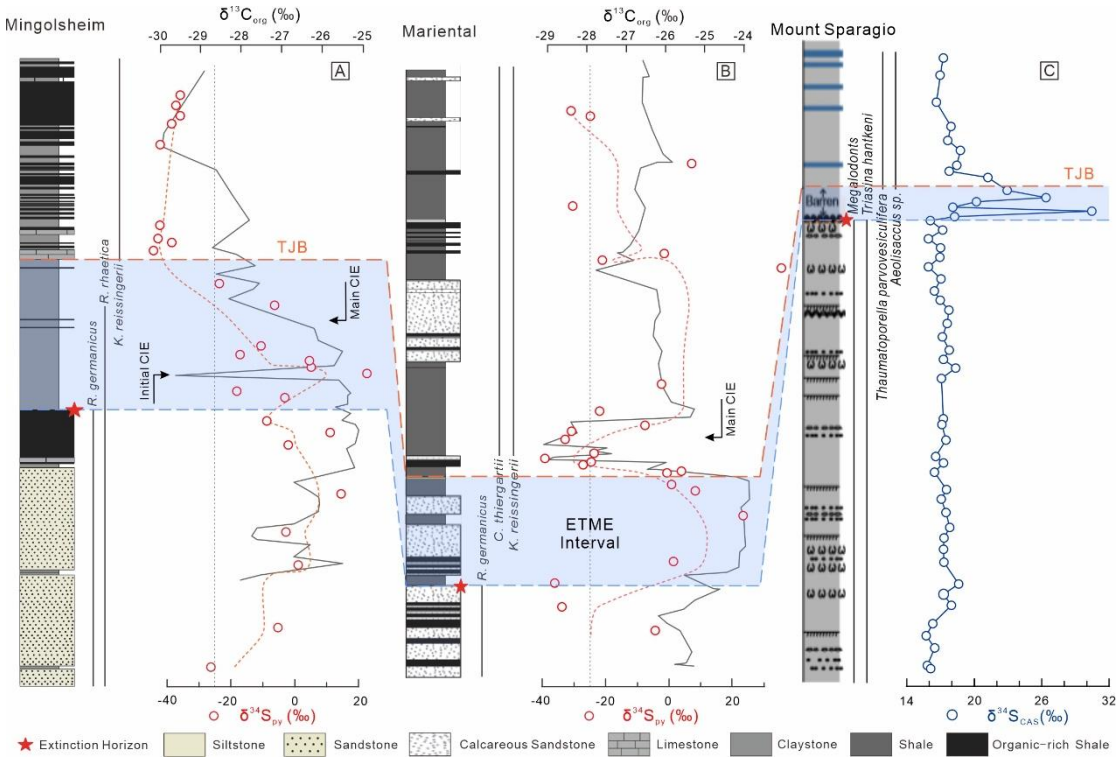

Fig. 8. Reported sulfur isotopes compositions of pyrite ($\delta^{34}S_{py}$) and carbonate-associated sulfur (CAS, $\delta^{34}S_{CAS}$). Stratigraphic logs and $\delta^{13}C_{org}$ data for the Mingolsheim and Mariental cores are after Quan et al. (2008) and van de Schootbrugge et al. (2008), respectively; $\delta^{34}S_{py}$ data for both cores are cited from Luo et al. (2018). Stratigraphic log, biostratigraphy information, and $\delta^{34}S_{CAS}$ data for the Mount Sparagio section are from He et al. (2020) and references therein.